This is the peer reviewd version of the followng article:

Thermal SZ fluctuations in the ICM: probing turbulence and thermodynamics in Coma cluster with Planck / Khatri, R., Gaspari, M.. - In: MONTHLY NOTICES OF THE ROYAL ASTRONOMICAL SOCIETY. - ISSN 0035-8711. - 463:1(2016), pp. 655-669. [10.1093/mnras/stw2027]

Terms of use:

The terms and conditions for the reuse of this version of the manuscript are specified in the publishing policy. For all terms of use and more information see the publisher's website.

14/11/2026 00:50

(Article begins on next page)

MNRAS **000**, 000–000 (0000) Preprint 5 September 2016 Compiled using MNRAS LATEX style file v3.0

Thermal SZ fluctuations in the ICM: probing turbulence and thermodynamics in Coma cluster with *Planck*

Rishi Khatri[1]⋆ and Massimo Gaspari[2]†
[1]*Department of Theoretical Physics, Tata Institute of Fundamental Research, Homi Bhabha Road, Colaba, Mumbai 400005 India*
[2]*Department of Astrophysical Sciences, Princeton University, 4 Ivy Lane, Princeton, NJ 08544-1001 USA*

5 September 2016

arXiv:1604.03106v4 [astro-ph.CO] 2 Sep 2016

ABSTRACT
We report the detection of thermal Sunyaev-Zeldovich (SZ) effect fluctuations in the intracluster medium (ICM) of Coma cluster observed with *Planck*. The SZ data links the maximum observable X-ray scale to the large Mpc scale, extending our knowledge of the power spectrum of ICM fluctuations. Deprojecting the 2-d SZ perturbations into 3-d pressure fluctuations, we find an amplitude spectrum which peaks at $\delta P/P = 33 \pm 12\%$ and $74 \pm 19\%$ in the $15'$ and $40'$ radius region, respectively. We perform tests to ensure fluctuations are intrinsic to the cluster and not due to noise contamination. By using high-resolution hydrodynamical models, we improve the ICM turbulence constraints in Coma, finding 3-d Mach number $\mathrm{Ma}_{3\mathrm{d}} = 0.8 \pm 0.3$ (15' region), increasing to supersonic values at larger radii (40'), and an injection scale $L_{\mathrm{inj}} \approx 500$ kpc. Such properties are consistent with driving due to mergers, in particular tied to internal galaxy groups. The large pressure fluctuations show that Coma is in adiabatic mode (mediated by sound waves), rather than isobaric mode (mediated by buoyancy waves). As predicted by turbulence models, the distribution of SZ fluctuations is log-normal with mild non-Gaussianities (heavy tails). The substantial non-thermal pressure support implies hydrostatic mass bias $b_M = -15\%$ to -45% from the core to the outskirt region, respectively. While total SZ power probes the thermal energy content, the SZ fluctuations constrain the non-thermal deviations important for precision cosmology. The proposed, novel approach can be exploited by multifrequency observations using ground based interferometers and future space CMB missions.

Key words: cosmology: cosmic microwave background – galaxies: clusters: intracluster medium – observations – theory – turbulence

1 INTRODUCTION

The *Planck* cosmic microwave background (CMB) mission (Planck Collaboration et al. 2011) has for the first time allowed us to retrieve all-sky maps (Planck Collaboration et al. 2015a; Hill & Spergel 2014; Khatri 2016) of the Sunyaev-Zeldovich effect (SZ; Zeldovich & Sunyaev 1969). The chief advantage of Planck over other past and current satellite and ground based missions is its multiple frequency channels covering the low frequency Rayleigh-Jeans as well as the higher frequency Wien region of the CMB spectrum making the separation of the thermal Sunyaev-Zeldovich from CMB and foregrounds feasible. As the blackbody photons from the CMB interact with hot intergalactic/intracluster medium (IGM, ICM) traveling from the last scattering surface (Sunyaev & Zeldovich 1970; Peebles & Yu 1970) to us, Compton scattering upscatters a fraction of photons to higher energy creating a distortion from the Planck spectrum I_ν^{Planck} (Sunyaev & Zeldovich 1972). The change in the intensity $\Delta I_\nu = I_\nu - I_\nu^{\mathrm{Planck}}$ of the CMB radiation is given by (Zeldovich & Sunyaev 1969)

$$\Delta I_\nu = y \frac{2h\nu^3}{c^2} \frac{x\mathrm{e}^x}{(\mathrm{e}^x-1)^2}\left[x\left(\frac{\mathrm{e}^x+1}{\mathrm{e}^x-1}\right)-4\right], \quad (1)$$

where $x = \frac{h\nu}{k_{\mathrm{B}}T}$, $T = 2.725(1+z)$ is the CMB temperature at redshift z, $\nu = \nu_0(1+z)$ is the frequency of CMB photon at redshift z, ν_0 is the observed frequency today ($z = 0$), h is the Planck's constant, k_{B} is Boltzmann constant and c is the speed of light. The amplitude of the distortion, y, is proportional to the integral of the pressure P along the line of sight,

$$y = \frac{\sigma_{\mathrm{T}}}{m_{\mathrm{e}}c^2}\int \mathrm{d}s\, n_{\mathrm{e}} k_{\mathrm{B}} T_{\mathrm{e}}, \quad (2)$$

where T_{e} and n_{e} are the electron temperature and electron number density respectively in the ICM plasma, m_{e} is the mass of the electron, σ_{T} is the Thomson scattering cross section, and s is the distance coordinate along the line of sight.

The Sunyaev-Zeldovich amplitude, y, contains information about the properties of the galaxy cluster which in turn are sensitive to the cosmological parameters. The *Planck* collaboration

⋆ E-mail: khatri@theory.tifr.res.in
† E-mail: mgaspari@astro.princeton.edu; *Einstein* and *Spitzer* Fellow

© 0000 The Authors

as well as independent groups have used the y maps created using the *Planck* data to study the clusters themselves as well as to measure the cosmological parameters (e.g., Hill & Spergel 2014; Planck Collaboration et al. 2015a,b,c; Ruan et al. 2015) In particular, the *Planck* collaboration has used the y parameter measurements of the Coma and Virgo cluster to constrain the average properties of these clusters (Planck Collaboration et al. 2013, 2015d). Since these nearby clusters are well resolved by *Planck*, detecting y signal out to several Mpc, it opens up the possibility of studying the y fluctuations – and hence the ICM pressure perturbations – on large scales, complementing the X-ray studies focusing on smaller scales (e.g., Schuecker et al. 2004; Churazov et al. 2012; Sanders & Fabian 2012; Gaspari & Churazov 2013; Gaspari et al. 2014a; Hofmann et al. 2016 and references within). The smallest scale we can study with *Planck* is limited by the angular resolution of $10'$ of the 100 GHz channel. We need the 100 GHz channel to be able to do component separation and minimize contamination from the other components.

While X-ray telescopes such as *Chandra* and *XMM-Newton* provide us with extensive details on the density and temperature of the ICM plasma ($T_{\rm x} \approx$ 1-10 keV), the X-ray emissivity is $\propto n_{\rm e}\, n_{\rm ion}$, where $n_{\rm ion}$ is the ion number density, i.e., limited to the core region due to the steep negative density gradient. The SZ signal can instead be detected with significance at much larger radii, granting the complementary view to X-ray observations. On the other hand, it should be noted that the temperature decline limits the SZ signal ($\propto n_{\rm e}\, T_{\rm e}$) at large radii too (Hallman et al. 2007). Using high-resolution 3-d simulations, Gaspari & Churazov (2013) and Gaspari et al. (2014a) have shown that the plasma perturbations in all the thermodynamic variables (density, entropy, pressure; ρ, K, P) are tightly related to the dynamical level of the cluster, i.e., how strong the turbulent motions are. In particular, the peak of the Fourier amplitude spectrum, $A_\rho(k_{\rm peak})$, of the relative *density* perturbations, $\delta\rho/\bar\rho$ is linearly tied to the 3-d Mach number of gas motions as (Gaspari & Churazov 2013)

$$\mathrm{Ma}_{\rm 3d} \approx 4\, A_\rho(k_{\rm peak}) \approx 2.4\, A_P(k_{\rm peak}), \tag{3}$$

where $\mathrm{Ma}_{\rm 3d} = \sqrt{3}\,\mathrm{Ma}_{\rm 1d} = \sigma_v/c_{\rm s}$, σ_v is the turbulent velocity dispersion, c_s is the ICM adiabatic sound speed and $\mathrm{Ma}_{\rm 1d}$ is the 1-d Mach number. In the last equality we have assumed adiabatic perturbations with adiabatic index $\gamma = 5/3$ and A_P is the amplitude of pressure fluctuations $\delta P/\bar P$. The cascade of the spectrum is instead related to the microphysics of the plasma. If thermal conduction (diffusion of internal energy via plasma electrons) is dominant, the density (or temperature) amplitude spectrum becomes steeper than that of the velocity field by up to factor of 5 (Fig. 2 in Gaspari et al. 2014a). For weaker diffusion, both slopes tend to the Kolmogorov power spectrum, $P_k \propto k^{-11/3}$ ($A_k \propto k^{-1/3}$). However, the density and velocity slopes do not follow each other linearly at progressively smaller scales, as thermodynamic quantities are not pure passive scalars. The simple analytic conversion in Eq. 3 between velocity and thermodynamic fluctuations should be thus used only near the injection scale (spectrum peak), i.e., between total variances.

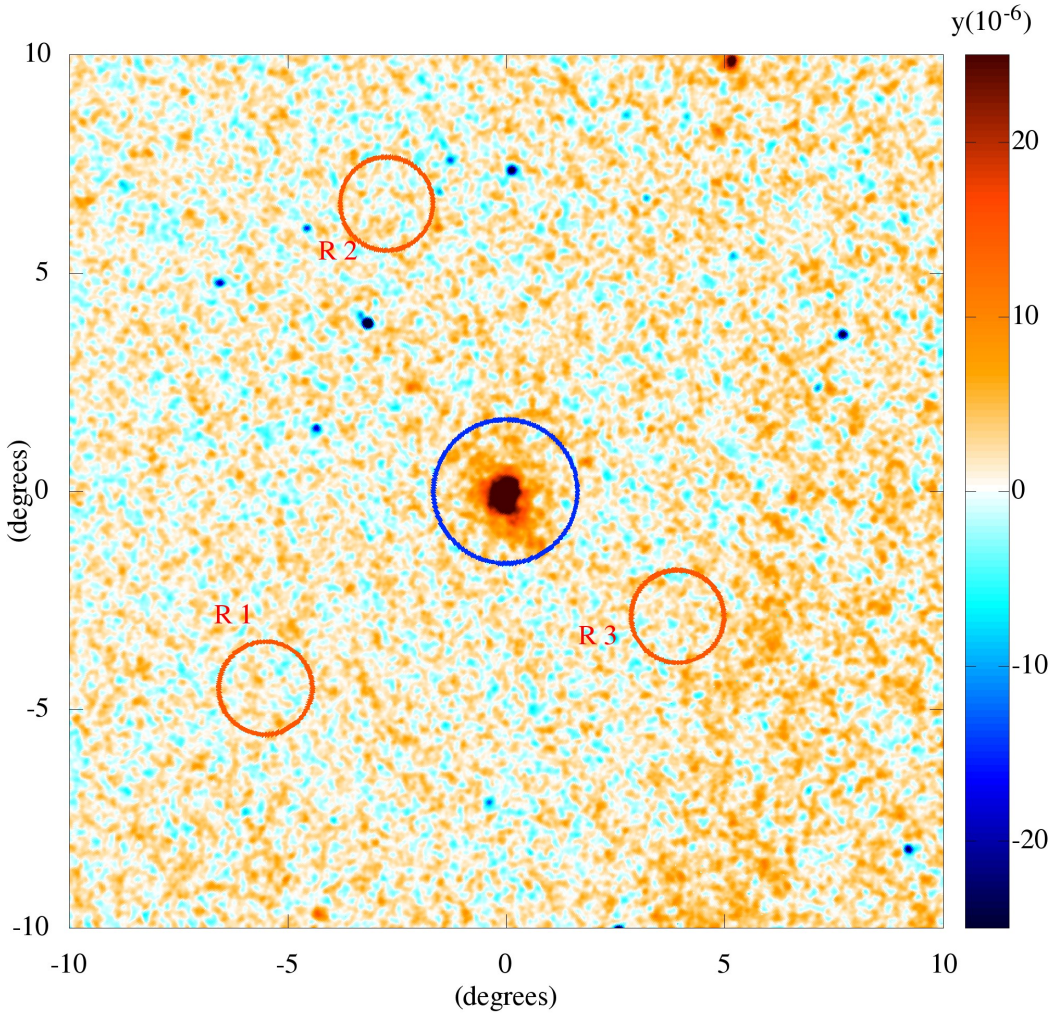
In this paper, we will for the first time use the Compton y fluctuations, $\delta y/y$, to retrieve pressure fluctuations $\delta P/P$, and thus assess the level of gas motions at scales larger than that probed via X-ray surface brightness in Coma galaxy cluster (Churazov et al. 2012; Gaspari & Churazov 2013). We will show that substantial *pressure* fluctuations ($\delta P/\bar P \simeq \gamma\, \delta\rho/\bar\rho$) of the order 30 percent are present at several 100 kpc, while gradually fading at radii $r \gtrsim 1$ Mpc. This implies gas turbulent motions[1] with Mach number $\mathrm{Ma}_{\rm 3d} \approx 0.8$, i.e., subsonic yet significant turbulence, as the average sound speed of Coma is $c_{\rm s} \approx 1500\,\mathrm{km\,s^{-1}}$. This is consistent with motions driven by mergers and cosmological flows (e.g., Lau et al. 2009; Vazza et al. 2009, 2011; Miniati 2014; Battaglia et al. 2015; Schmidt et al. 2016).

It is crucial to understand the physics of the ICM, as hot gaseous haloes have been found to be ubiquitous from massive galaxy clusters to elliptical and spiral galaxies (e.g., Anderson et al. 2015). Remarkably, the cascading large-scale turbulence in the hot halo can also drastically alter the accretion mode onto the central supermassive black hole, igniting 'chaotic cold accretion' (e.g., Gaspari et al. 2015). The presence of significant non-thermal pressure support has important implications not only for the diffuse gas physics, but also for cosmology. Being the largest collapsed structures, galaxy clusters are highly sensitive to the cosmological parameters. To achieve high-precision cosmology, however, we require precise estimates of the cluster masses, minimizing errors and scatter. The usual approach of using the average SZ and X-ray signal, which can only give an estimate of thermal pressure support, gives a biased estimate of the cluster mass. This bias, which comes from the non-thermal pressure contributions (assuming hydrostatic equilibrium[2]), has been typically estimated by using numerical simulations (e.g., Dolag et al. 2005; Vazza et al. 2011; Iapichino et al. 2011; Battaglia et al. 2012; Nelson et al. 2014; Biffi et al. 2016 and references within). The non-thermal pressure has also been studied using analytical methods guided by both simulations and observations (e.g., Chaudhuri et al. 2012, 2013; Shi et al. 2015). Observationally the evidence for the non-thermal pressure support is indirect via the discrepancy between the X-ray, SZ or dynamical masses and the masses derived via weak or strong lensing (e.g., Mahdavi et al. 2008; Zhang et al. 2010; von der Linden et al. 2014; Smith et al. 2016). Radio observations can constrain the magnetic field strength via Faraday rotation measure, which is typically a few μG (e.g., Ferrari et al. 2008; Bonafede et al. 2010), and thus can estimate the magnetic pressure role. The SZ fluctuations open up the possibility to directly probe the turbulence contribution to the non-thermal pressure support, which we expect to be dominant from cosmological simulations (e.g., Avestruz et al. 2016).

For the first exploratory study, we choose Coma cluster. Coma (or Abell 1656) is one of the biggest clusters in angular size visible to us with highest signal to noise ratio in *Planck* data and in a relatively uncontaminated part of the sky. It is thus the ideal object to start looking for y-fluctuations which are expected to be weaker than the average y signal. The Coma cluster is situated at a redshift of $z = 0.0232$ (Abell et al. 1989). The physical distance depends on the cosmological parameters and we take the distance of the Coma cluster to be 93 Mpc (choosing the same cosmology as in Churazov et al. 2012). At this distance $10' = 270.5$ kpc and $40' \approx 1$ Mpc. A crude estimate of the virial radius is $R_{200} \approx 2\,R_{500}$, where $R_{500} = 1.31$ Mpc. Coma is classified as a hot, massive galaxy cluster ($M_{\rm vir} \approx 10^{15}\,\mathrm{M_\odot}$) with average core plasma temperature 8.5 keV and electron density $n_{\rm e} \simeq 4{\times}10^{-3}\,\mathrm{cm^{-3}}$, which decreases to $10^{-4}\,\mathrm{cm^{-3}}$ at R_{500} (cf. *XMM* profiles in Gaspari & Churazov 2013, Fig. 1). Coma is an archetypal non-cool-core cluster with radiative cooling time greater than the Hubble time. The main objective of

[1] Turbulence should be here interpreted as large scale eddies, sometimes referred to as 'bulk motions' given the long turnover timescale.

[2] Part of the bias may come from deviations from spherical symmetry or failure of hydrostatic equilibrium assumption.



[!ht]

Figure 1. We show $20^\circ \times 20^\circ$ region centered on the Coma cluster in LIL map. The $R_{200} \approx 2.62$ Mpc region is marked with a circle at the center of the map. The three 1° regions used to test for typical contamination in this part of the sky are also marked with circles and labeled $R1, R2, R3$. The bright cluster at the top-right edge of the plot is ACO 1795.

the current investigation is finding the level of SZ fluctuations and SZ power spectrum of Coma cluster, carefully assessing the role of projection and contamination, and to provide the first exploratory analysis which can be leveraged and extended by future SZ surveys. The paper is organized as follows. In §2, we describe how to retrieve SZ fluctuations from *Planck* data on top of the average y profile. In §3, we deproject the y (2-d) power spectrum into the 3-d power spectrum of pressure perturbations, $\delta P/P$. In §4, we discuss the key physical implications arising from SZ fluctuations, focusing on ICM turbulence constraints, thermodynamics, and the mass bias related to non-thermal pressure. In §5, we summarize the main conclusions and discuss future prospects.

2 SZ FLUCTUATIONS IN COMA CLUSTER

The *Planck* collaboration has released the Sunyaev-Zeldovich effect maps (Planck Collaboration et al. 2015a) calculated from two different algorithms NILC (Needlet Internal Linear Combination) (Delabrouille et al. 2009) and MILCA (Modified Internal Linear Combination Algorithm; Hurier et al. 2013). Several independent groups have also used *Planck* data to construct the SZ effect maps (Hill & Spergel 2014; Khatri 2016). We will use the MILCA and NILC maps as well as the SZ map from Khatri (2016) based on pixel based parameter fitting algorithm LIL (Linearized Iterative Least-squares) developed in Khatri (2015). The main difference between the *Planck* collaboration maps and our LIL map is that in MILCA/NILC, which use internal linear combination methods, the local monopole is removed while LIL preserves the monopole or the average SZ signal. In addition, the ILC methods determine the contamination spectrum from the data separately in different parts of the sky and try to remove all contamination components including the CO emission. The LIL method on the other hand ignores the CO emission and fits for a parametric contamination model in each pixel in the sky. This is not a problem as the CO emission is negligible in the Coma region of the sky. We refer to Khatri (2016) for detailed comparison of LIL with NILC/MILCA algorithms. We will use all three, NILC, MILCA and LIL, maps for our analysis. As we will see, all three methods agree and choosing one map over the other does not affect our results and conclusions. The three maps, calculated with different algorithms, have different levels of contamination from other components. The comparison of LIL maps

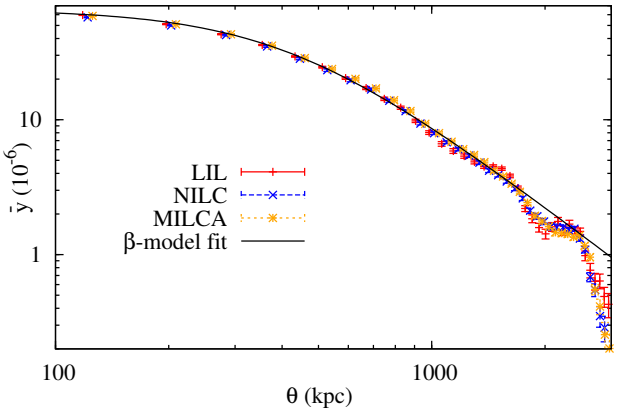


Figure 2. The measured y profile of Coma cluster in different y maps (Sec. 2) and the best fit β-model profile to the LIL map. The points for LIL and MILCA have been slightly offset from the center of the bin in the x direction to make them easily distinguishable. The distance to Coma of 93 Mpc is used. The size of a bin is 3′ or 81 kpc.

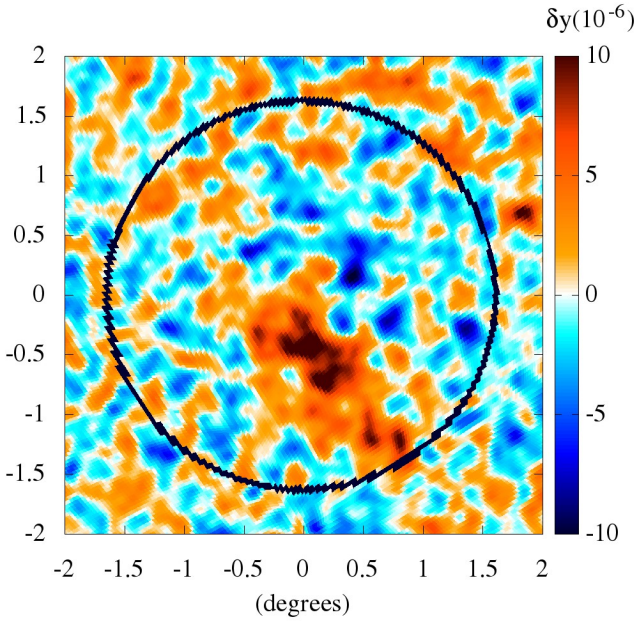


Figure 3. Fluctuations (LIL map) of y, $\delta y(\boldsymbol{\theta})$ in Coma cluster with the average profile, estimated in rings of 3 arcmin and linearly interpolated, subtracted. The circle marks $R_{200} \approx 2.62$ Mpc region of the Coma cluster.

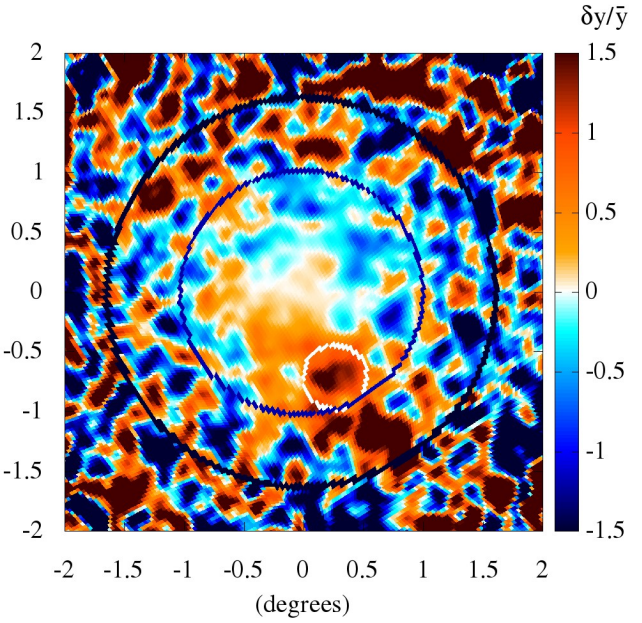


Figure 4. Fractional fluctuations of y (LIL map), $\delta y(\boldsymbol{\theta})/\bar{y}$ in Coma cluster. The outer circle marks $R_{200} \approx 2.62$ Mpc region of the Coma cluster. The inner blue circle marks 60′ radius. The white circle with radius 15′ encloses the group of galaxies NGC 4839. The fluctuations become nonlinear as we move away from the the center of the cluster.

with NILC/MILCA maps serves as a test against non-SZ contamination.

The average SZ and pressure profiles and related properties of the Coma cluster have been studied in detail in Planck Collaboration et al. (2013). We are interested in the fluctuations in the SZ signal and related ICM pressure. To study the fluctuations in SZ, $\delta y(\boldsymbol{\theta})/\bar{y}(\theta)$, we want to remove the average profile $\bar{y}(\theta)$, where $\boldsymbol{\theta}$ is the two dimensional position vector in the plane of the sky and θ is its magnitude or the distance from the center of the cluster. We assume spherical symmetry, so that $\bar{y}$ depends only on the radial distance θ. As can be seen in Fig. 1, such an assumption is a fair approximation. The 2-d to 3-d deconvolution (Abel transform) can be done exactly only under the assumption of spherical symmetry since the projection invariably leads to loss of information. Although there have been studies to correct for the asphericity when doing a statistical study involving large number of clusters (e.g. Fox & Pen 2002), such an attempt for a single cluster would be highly sensitive to the model of asphericity used. This is especially clear from Fig. 1 where it can be seen that the departure from sphericity is non-trivial and it is a matter of choice what part of the anisotropy we assign to the departure of average model from sphericity, i.e. the static background, and what part we assign to dynamical processes such as mergers and turbulence.

We extract the average profile, $\bar{y}$, by averaging in rings of width 3 arcmin around the SZ peak in the Coma cluster at galactic coordinates $(l = 57.3°, b = 87.99°)$[3]. The profile is shown in Fig. 2 for NILC, MILCA and LIL maps. Since LIL also has monopole contribution from background SZ signal, we have subtracted an estimated $y_{\rm background} = 10^{-6}$ from the profile (Khatri & Sunyaev 2015). The β-model has been found to be a good fit to the SZ profile in South Pole Telescope (SPT) clusters (Plagge et al. 2010). Defining the β-model as

$$\bar{y}_\beta(\theta) = \frac{y_0}{(1+\theta^2/\theta_c^2)^\beta} \tag{4}$$

[3] This is approximately half a pixel ($\sim 0.5'$) away from the center used by *Planck* collaboration. Such a difference is much smaller than the map resolution and does not affect the results.

we get the best fit values to the LIL profile at $\theta < 1200$ kpc of $y_0 = (65.5 \pm 0.31) \times 10^{-6}$, $\theta_c = (419.6 \pm 9.26)$ kpc, $\beta = 1.07 \pm 0.024$ where θ is the radial distance from the center of the cluster in the 2-d plane of the sky. At $\theta \gtrsim 1200$ kpc we see a deviation from the β-profile. In particular, the flattening in the observed profile at ~ 2000 kpc coincides with the recently reported identification of a shock in the SZ map of Coma at a distance of ~ 75' from the center by Erler et al. (2015). We note that this feature is absent from the profile reported by Planck Collaboration et al. (2013). However the radial bins used by Planck Collaboration et al. (2013) are much larger than the size of this feature and it is most likely averaged out in their profile. For comparison[4], the X-ray surface brightness profile of Coma has core radius of 272 kpc and steeper slope, $\mathrm{SB_x} \propto (1+\theta^2/\theta_c^2)^{-1.75}$; Gaspari & Churazov (2013). If we assume spherical symmetry, we can get the pressure profile from the SZ profile using Abel transform,

$$\bar{P}(r) = \frac{m_e c^2}{\sigma_T} \frac{1}{\pi} \int_\infty^r \frac{\mathrm{d}y}{\mathrm{d}\theta} \frac{\mathrm{d}\theta}{(\theta^2 - r^2)^{1/2}} = \frac{P_0}{(1 + r^2/r_c^2)^{\beta+1/2}}, \quad (5)$$

where r is the radial distance from the center in 3-d, $r^2 = \theta^2 + z^2$, z is the distance along the line of sight direction and

$$P_0 = \frac{m_e c^2}{\sigma_T} \frac{y_0}{r_c} \frac{\Gamma(\beta + 0.5)}{\sqrt{\pi}\Gamma(\beta)}, \quad (6)$$

where Γ is the usual gamma function.

We will use the $\beta-$model fit of the profile to just simplify the calculation of the window functions that will come up when we calculate the fluctuations. To extract the final relative perturbations, we subtract instead the actual *measured* average profile $\bar{y}$, linearly interpolated between the bins from the total signal y to get the map of y fluctuations, $\delta y(\boldsymbol{\theta}) = y(\boldsymbol{\theta}) - \bar{y}$. This way we are not dependent on the arbitrary choice of an idealized model (e.g., β- or Arnaud profile). The map of δy is shown in Fig. 3 in a $2^\circ \times 2^\circ$ region around the Coma cluster for LIL map and the fractional fluctuations $\delta y/\bar{y}$ are shown in Fig. 4. The β-model fit will however be useful when we test for contamination in our results.

We will calculate the angular power spectra using the publicly available software PolSpice (Szapudi et al. 2001; Chon et al. 2004) which also calculates the covariance matrix. The calculation is similar to Hivon et al. (2002) and Tristram et al. (2005) but is done in correlation space instead of harmonic space which makes the deconvolution of masks much faster. We convert the angular power spectrum to Fourier power spectrum using the flat sky approximation (Jaffe & Kamionkowski 1998). See Appendix A for a short derivation and also for the definition of our Fourier transform convention which differs from that in Churazov et al. (2012); Gaspari & Churazov (2013). The *Planck* collaboration provides half-ring maps which have the same signal as well as almost the same noise amplitude but the noise between them is uncorrelated. We will use the cross-power spectra of half-ring y-maps so that the uncorrelated white noise is automatically canceled. All the power spectra in this paper have been corrected for the effect of the masks and the 10′ FWHM (full width half maximum) beam of the SZ maps.

[4] X-ray studies use a different β' definition starting from the density profile $\rho \propto (1 + r^2/r_c^2)^{3\beta'/2}$. The projected *isothermal* profile for y would then be $\propto (1 + \theta^2/\theta_c^2)^{1/2-3\beta'/2}$, i.e., $\beta' = (2\beta + 1)/3 \simeq 1.05$ for Coma. the X-ray brightness profile is instead $\propto (1 + \theta^2/\theta_c^2)^{1/2-3\beta'}$, which is steeper as X-ray emissivity $\propto \rho^2$. Coma X-ray data fits $\beta' \simeq 0.75$; such discrepancy with SZ arises because the isothermal assumption is violated outside the core.

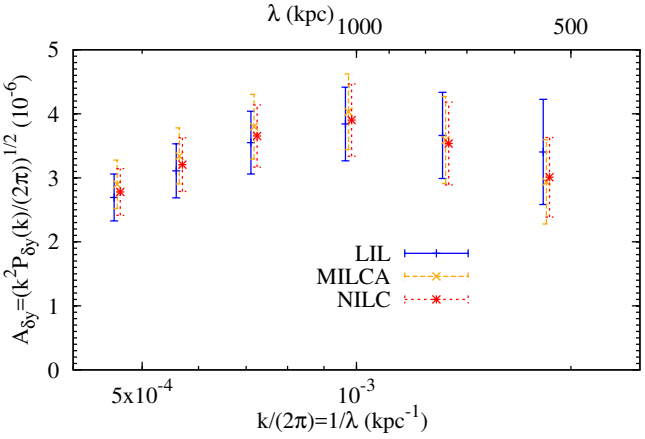


Figure 5. Power spectrum of fluctuations of y, $\delta y = y - \bar{y}$, in Coma with the average profile subtracted for MILCA,NILC and LIL maps. The NILC data point is at the center of the k bin while the other data points are slightly offset to make them distinguishable from each other.

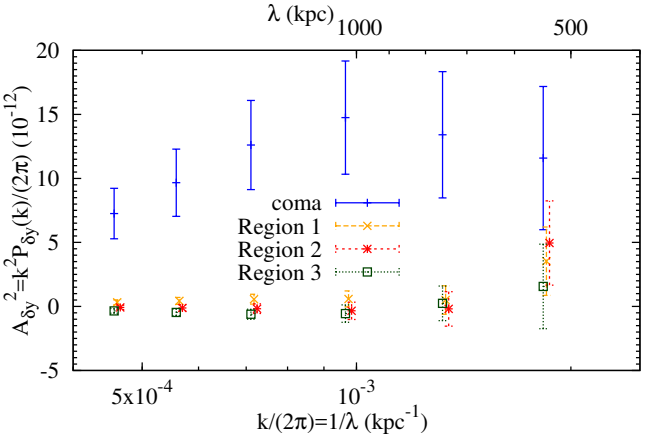


Figure 6. Power spectrum of fluctuations of y, $\delta y = y - \bar{y}$, in Coma and three test regions around Coma in LIL map. Note that the cross power spectrum between the two half ring maps in the test regions is in fact negative for all points except the last indicating that these test regions are dominated by noise. The errors are dominated by sample variance and are therefore proportional to the power spectrum on large scales for same binning.

We show the power spectrum of the Coma SZ fluctuations, $\delta y = y - \bar{y}$ in LIL, MILCA and NILC maps in Fig. 5 calculated after masking the rest of the sky. The amplitude $A_{\delta y}$ of the power spectrum $P_{\delta y}$ is plotted. The mask is a map consisting of 1s in the region occupied by Coma and 0s everywhere else which leaves 60′ radius region at the position of the Coma cluster unmasked. We apodize the mask before multiplication with the y-map to avoid high frequency artifacts in power spectrum due to the sharp edge in the mask. The apodization is done using a 15′ Gaussian replacing the 1s in the mask by $1 - \exp\left(-9\theta^2/(2\theta_{\rm ap}^2)\right)$ with $\theta_{\rm ap} = 15'$. All three maps agree very well. There is slightly larger noise in LIL map which shows up as bigger error bar in the smallest scale bin. The bin sizes were chosen to be large enough to minimize the correlation between the neighbouring bins, which are expected when we do not

have full sky, and small enough so that there are enough bins that the shape of the power spectrum is not washed out.

It is interesting to note there is a maximum at 1 Mpc ($\sim R_{500}$) and a decline, which corroborates the idea (§3) that this scale is the dominant dynamical scale, even for absolute fluctuations – such scale is commonly associated with major mergers and cosmological filamentary inflows. This interpretation comes with a caveat. On small scales we expect suppression of power because of the integration along the line of sight which suppresses small scale power in the 2-d projected map. On large scales we expect decrease in power because the outskirts of the cluster become important and there the amplitude of the average SZ signal declines. In particular, the above mentioned effects would shift the peak in the projected power spectrum. The peak is on the same scale as the large fluctuation visible slightly off center in the δy map in Fig. 5.

In order to test that the fluctuations we are seeing are intrinsically from the cluster and not SZ effect from background sources or contamination, we randomly select three test regions near the Coma cluster, but at least few degrees away from both Coma and Virgo clusters. Since there is no dominant cluster in these regions, any fluctuations would be dominated by background SZ signal and contamination. The regions chosen are at similarly high galactic latitudes and so should have the similar magnitude of contamination. The centers of the three test regions in galactic coordinates (l, b) are $(171.6, 84.0)$, $(75, 81.0)$ and $(315, 86.0)$ and we will label them as "region 1/R 1", "region 2/R 2", and "region 3/R 3" respectively, as shown in Fig. 1.

We apply the same procedure that we used to calculate the fluctuation power spectrum of Coma to these three regions. The results are shown in Fig. 6 for the LIL map. We expect that all contamination and non-Coma signal in the Coma regions would be similar to that in the test regions. From our null test in Fig. 6 we see that our power spectrum is dominated by the SZ anisotropies originating in Coma. The last bin is affected by contamination (at $1\sigma - 2\sigma$ level) giving a positive signal in the test regions; at the smallest scale, we thus expect some contribution from contamination, albeit not fully overwhelming the intrinsic Coma signal. We note that this test just shows the typical contamination in this part of the sky is small compared to our signal. The actual contamination in the Coma cluster could be smaller since we expect the galactic contamination to be smaller, or could be larger if there are additional radio and infrared point sources in the Coma cluster that we cannot account for by looking at other regions of the sky. The contribution of the point sources to the NILC, MILCA and LIL maps is very different (Khatri 2016) with NILC probably the cleanest in this respect. The fact that the results from the three maps agree so well with each other gives us confidence that the contribution of point sources and other extra-galactic and galactic contamination is negligible. Also, there are no strong point sources detected in the region of interest in the Planck point source catalogs (Planck Collaboration et al. 2015e).

3 PRESSURE FLUCTUATIONS IN COMA CLUSTER

We want to calculate the 3-d power spectrum of fractional pressure fluctuations $\delta P/P$. We can write the 2-d SZ power spectrum, P_y, as a convolution of the 3-d pressure power spectrum P_P with a window function (Appendix B for a derivation; see also Peacock 1999) as

$$P_y(k_\theta) = \int \frac{\mathrm{d}k_z}{2\pi} \left|\tilde{W}(k_z)\right|^2 P_P\left(|\mathbf{k}_\theta + \mathbf{k_z}|\right), \tag{7}$$

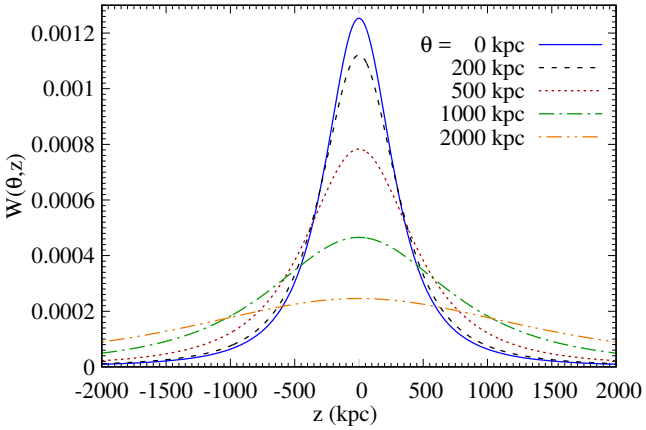


Figure 7. The window function $W(\theta, z)$ at several values of the projected distance θ from the center. As we get away from the center, the window profile becomes broader increasing the suppression of the small scale power.

where P_y is the power spectrum of fractional y fluctuations $\delta y/\bar{y}$, P_P is the power spectrum of fractional pressure fluctuations, $\delta P/\bar{P}$, $\mathbf{k}_\theta$ is the Fourier vector in the 2-d x-y plane of the sky and $\mathbf{k_z}$ is the Fourier vector along the line of sight direction $\hat{\mathbf{z}}$, non-bold quantities are the scalar amplitudes of the corresponding vectors and $\tilde{W}(k_z)$ is the Fourier transform in the $\hat{\mathbf{z}}$ direction of the weight function defined by

$$W(\boldsymbol{\theta}, z) \equiv \frac{m_\mathrm{e}c^2}{\sigma_\mathrm{T}} \frac{\bar{P}(\boldsymbol{\theta}, z)}{\bar{y}(\boldsymbol{\theta})}, \tag{8}$$

with $\boldsymbol{\theta} = (\theta_x, \theta_y)$ is the position vector in the x-y plane of the sky in the flat sky approximation so that its magnitude θ is the projected distance from the center of the cluster. Note that the window function, plotted in Fig. 7 in real space for several values of projected distance θ for the best fit β-model profile, is in general a function of position on the sky, $\boldsymbol{\theta}$, which we have ignored in deriving the equation 7. This is a good approximation for the central part of the cluster. We show in Fig. 8 the Fourier space window function $|\tilde{W}(k_z)|^2$ at several values of projected distance θ from the center of Coma calculated using our best fit profiles in Eqs. 4 and 5. Assuming $|\tilde{W}(k_z)|^2$ to be independent of θ is therefore a rough approximation which becomes more and more accurate as we confine ourselves to the smaller and smaller projected region of the cluster.

We can further simplify Eq. 7 if we confine ourselves to small scales so that $k_z \ll k_\theta$. We see from Fig. 8 that the window function drops very sharply on small scales and the contribution to the convolution integral from $k_z/(2\pi) \gtrsim 5\times10^{-4}$ kpc^{-1} would be small justifying this approximation for physical scales $\lesssim 2000$ Mpc. In this limit, the relation between 2-d SZ power spectrum and 3-d pressure power spectrum reduces to (Churazov et al. 2012)

$$\begin{aligned} P_y(k_\theta) &\approx P_P\left(k_\theta\right) \int \frac{\mathrm{d}k_z}{2\pi} \left|\tilde{W}(k_z, \theta)\right|^2 \\ &\approx N(\theta)\, P_P\left(k_\theta\right). \end{aligned} \tag{9}$$

For $\theta = \{0, 100, 200, 500, 1000, 2000\}$ kpc we get $N = \{7.4, 7.2, 6.6, 4.6, 2.7, 1.4\} \times 10^{-4}$ respectively. We can check the last approximation explicitly by using an input 3-d power spectrum and performing the convolution integral. For a power law power spectrum exponentially cut off at small and large scales, $P_p(k) = k^{-n} \exp\left(-k_c/k\right) \exp\left(-k\right)$, we show the ratio of 3-d to 2-d power spectrum in Fig. 9 for different parameters n and k_c and

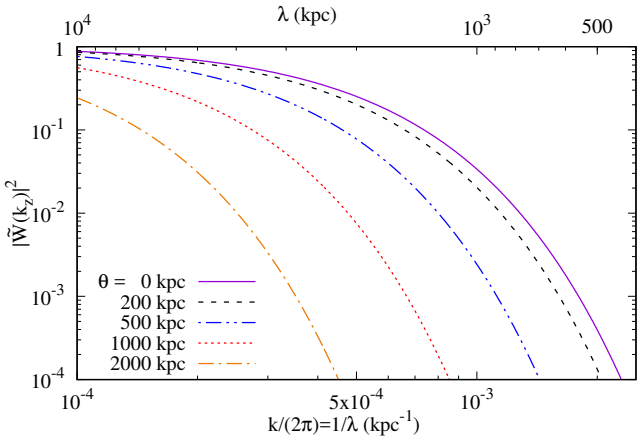


Figure 8. The window function $|\tilde{W}(k_z)|^2$ at several values of the projected distance θ from the center. As we get away from the center, the window profile becomes broader increasing suppression of the small scale power.

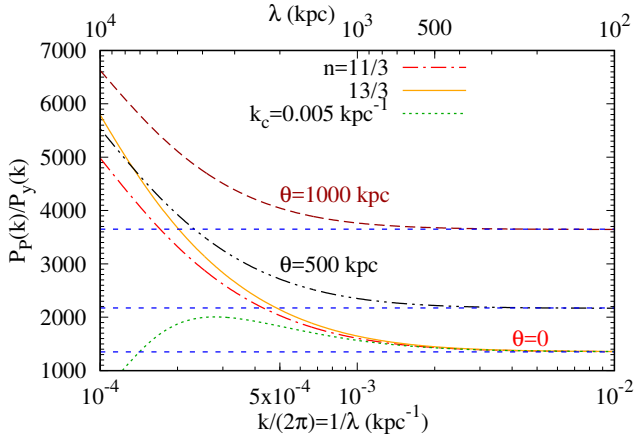


Figure 9. The ratio of pressure (3-d) to SZ (2-d) power spectra for different 3-d power spectra and projected radial distances θ. The default values for all curves unless specified are $k_c = 10^{-3}$ kpc^{-1} and $n = 11/3$. The Eq. 9 approximation is shown as the horizontal line.

different projected distances. The default values are $n = 11/3$ and $k_c = 10^{-3}$ kpc^{-1} unless specified otherwise. The approximation in Eq. 9 is quite accurate on small scales but starts to deteriorate on large scales where it is sensitive to the exact form of the power spectrum, in particular the cutoff scale k_c. Because of the information lost in projection it is impossible to accurately deconvolve the power spectrum; we will thus use for the rest of the paper the approximation in Eq. 9 with $N = 7\times10^{-4}$. Although in terms of power spectral density P_k the ratio N appears to be large, if we consider the amplitude spectrum A_k (Eq. C3) – which is dimensionless having the same units as the corresponding real space perturbation and is the power per unit logarithmic k interval – the $A_P(k)/A_y(k)$ ratio remains near unity at large scales, increasing only by a factor of a few for scales smaller than 500 kpc (see Fig. 10).

We now have all ingredients to calculate the power spectrum of SZ fluctuations for Coma and use Eq. 9 to scale the 2-d SZ fluctuation power spectrum to 3-d pressure fluctuation power spectrum. We first divide the SZ fluctuation map of Fig. 3 by the average profile to get a map of fractional perturbations of SZ shown in Fig.

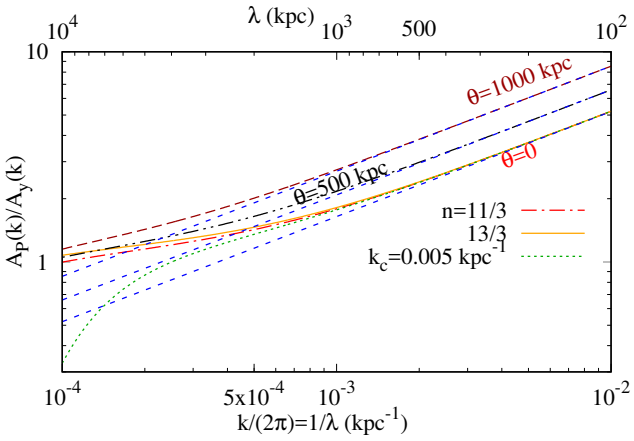


Figure 10. The ratio of pressure (3-d) and SZ (2-d) fluctuations amplitude spectrum for different 3-d power-law slopes and projected distances θ. The Eq. 9 approximation is shown as the straight lines. Note that the amplitude ratio remains near unity at large scales, regardless of projection effects. For a comparison to the X-ray window see Zhuravleva et al. (2012). The green curve uses an aggressive exponential cutoff for illustrative purposes; more likely, the 3-d spectrum merges with the cosmological power spectrum on scales larger than the cluster size, which is beyond our reach.

4. Since the profile $\bar{y} \to 0$ at large distances from the center, the fractional fluctuations, $\delta y/\bar{y}$ would diverge and far from the cluster the noise and contamination would start getting amplified and will dominate the overall power spectrum. The power spectrum is therefore a strong function of the maximum radius we decide to use for calculating the power spectrum. We show in Fig. 11 the power spectrum of pressure fluctuations, $\delta P/\bar{P}$, for different values of maximum radius from the center of Coma, $\theta_{\rm max}$, i.e. we mask the regions beyond the maximum radius in the map leaving only the region $\theta < \theta_{\rm max}$ unmasked. We further apodize the mask with $\theta_{\rm ap} = 15'$ Gaussian as defined in the previous section for $\theta_{\rm max} > 30'$ and use $\theta_{\rm ap} = 5'$ for $\theta_{\rm max} \leqslant 30'$[5]. We note that formally we retrieve electron pressure via SZ signal, however, since we are only interested in relative fluctuations, the ion component is secondary here. Moreover, Gaspari & Churazov 2013 found that the ion and electron temperature differ only by 1 - 15 percent (core to outskirts, respectively) in typical ICM turbulence simulations. Note that the errors on large scales are dominated by the sample variance. The sample variance is a function of bin size and for large bin size the variance does not rise as fast on large scales as we would expect for unbinned or logarithmically binned data since we are averaging many modes even on large scales.

As expected, the fluctuations when normalized to the average profile $\bar{P}$ are larger when we use a larger extraction radius. For comparison, we show the amplitude of density fluctuations retrieved from the latest *Chandra* X-ray observation (Gaspari & Churazov 2013; updated version of the data shown in Churazov et al. 2012)[6]. Our smallest extraction radius of 15' is larger than the half-size of

[5] Apodization is beneficial for reducing the edge effects while calculating the power spectrum, but it should not be so large that most of the signal is obscured. Large apodization implies using less data, hence larger error bars.
[6] As in Gaspari & Churazov (2013), we prefer to compare only with the more robust and improved *Chandra* data, as *XMM* has 40× lower on axis angular resolution. There are, in addition, systematic differences between Chandra and XMM instrument (e.g. Schellenberger et al. 2015)

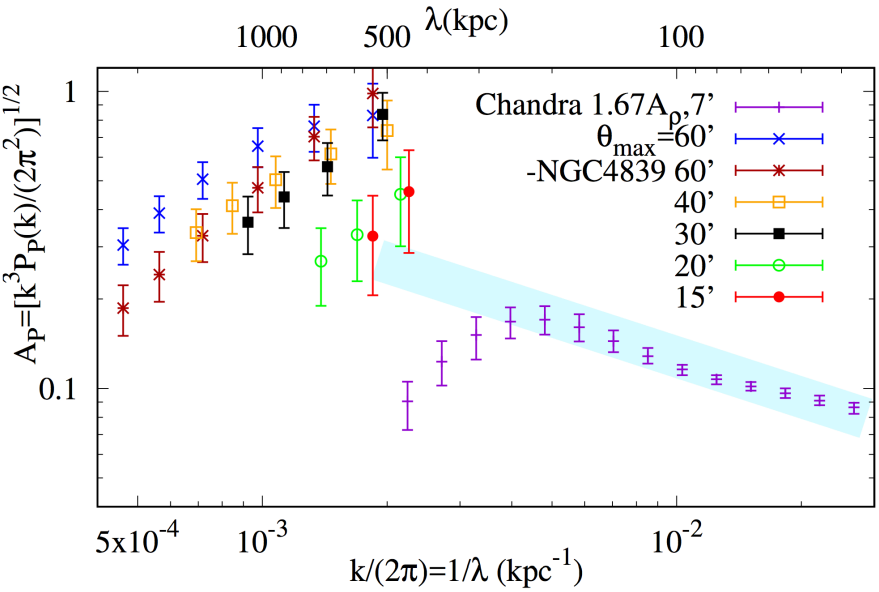


Figure 11. Amplitude spectrum of pressure fluctuations for varying extraction radius $\theta_{\rm max}$ (LIL maps), for *Planck* and *Chandra* data (violet; Gaspari & Churazov 2013). This key plot shows that large radii have significantly larger perturbations, and thus stronger turbulence motions ($\rm Ma_{3d} \gtrsim 0.8$), consistently with cosmological mergers and inflows. The injection scale is constrained to be at $\approx$ 500 kpc, given the decline of amplitude at small k. The power spectrum labeled "-NGC4839 60' " is obtained by masking 15' radius region with 15' apodization centered on the NGC 4839 group of galaxies. Note that the *Chandra* power spectrum is calculated in box of half-size 7' which is below the Planck resolution. The half-size of the box at the Coma distance is $\sim$ 200 kpc which coincides with the peak in the X-ray derived power spectrum. The SZ and X-ray data thus probe mutually exclusive different regions of the cluster (outer and inner part, respectively). Extrapolating the *Chandra* inertial range (cyan band) shows the 2 datasets are consistent within errors in the inner extraction region.

the X-ray extraction region of 7'. This fact combined with our SZ map resolution of 10' means we are probing different regions of the Coma cluster in SZ and X-rays. In the smallest disc we have also non-negligible contribution from contamination. The amplitude is however still consistent with γA_ρ within 2-σ, where A_ρ is the 3-d amplitude of power spectrum of density fluctuations $\delta\rho/\bar{\rho}$ from *Chandra*, and $\gamma = 5/3$ is the adiabatic index (§3.1 for the discussion). We point out that the decrease in the large scale power in X-ray data is an artifact of approaching the limited box size. This becomes clear when we compare the *Chandra* and *XMM* data in Churazov et al. (2012) (their Fig. 13). The *XMM* box size is 12' and the downturn in power spectrum happens at larger scales in the *XMM* data compared with the *Chandra* data. There is also discrepancy on large scales between the *XMM* and *Chandra* pointing to systematic effects related to the box size (see Fig. 14 in Churazov et al. 2012). E.g., above 300 kpc, Churazov et al. (2012; section 5.1) claim a factor of 2 uncertainty in systematic errors. If we extrapolate our amplitude to the core size of 7' probed by X-ray observations, the agreement between the X-ray and SZ improves. Similarly, if we extrapolate the X-ray cascade to several 100 kpc scale, the inertial range joins the SZ green and red points within errorbars (cyan band). Keeping in mind the discussed uncertainties and the fact we are probing different extraction regions of the cluster, the SZ results are consistent with the X-ray data.

The 60' radius region includes the group of galaxies NGC 4839 which is falling into the Coma cluster (Briel et al. 1992; Neumann et al. 2001). This group is marked with a white circle in Fig. 4 and shows up as a bright spot in the normalized fluctuations. To estimate the contribution of this group to the fluctuation signal, we mask 15' radius region around the hot spot (which coincides with the X-ray source in ROSAT all sky survey; Briel et al. 1992). In addition we apodize the combined mask for the 60' region analysis with 15' Gaussian as explained above, down-weighting the contribution from extended 15'-30' radius region around the group. Comparison of the two 60' power spectra – with and without masking the group – shows that the contribution from the group is small, decreasing the amplitude at large scales by 20 - 30 percent. We note that the group lies outside the 30' radius and, taking into account the fact that we extend our masks by apodization, it does not contribute to the fluctuations calculated in the 40' and smaller radius regions. It should also be noted that the hot plasma is volume filling within the cluster and internal groups. So cutting regions of the sky will inevitably also remove some turbulence perturbations intrinsic to Coma.

To test whether we are seeing actual anisotropies from Coma or the contamination from non-Coma background SZ or foregrounds, we again use our test regions. We compare the test regions in LIL and NILC maps with the Coma region in LIL, NILC and MILCA maps in Fig. 12 for $\theta_{\rm max} = 60', 30', 20', 15'$. We plot A_k^2 in these plots since when we are dominated by noise in the test regions the cross spectrum between the two half-ring maps can take negative values. We see that in Fig. 12 (top) we can attribute all signal measured in the Coma region to the anisotropies in the Coma cluster except in the last bin where the contamination may have a subdominant contribution. Note that as we take the cross-spectrum, the noise cancels out in the mean signal but still contributes to the error bars, which are thus increasing toward the resolution limit. For our smallest disc with radius $\theta_{\rm max} = 15'$ (Fig. 12, bottom) we can measure only the smallest scales and here our measured power in Coma is of similar magnitude as the test regions. The NILC map test regions have however smaller contamination, while the signal in NILC is consistent with that in the LIL and MILCA maps. We therefore have evidence of pressure fluctuations even in the central

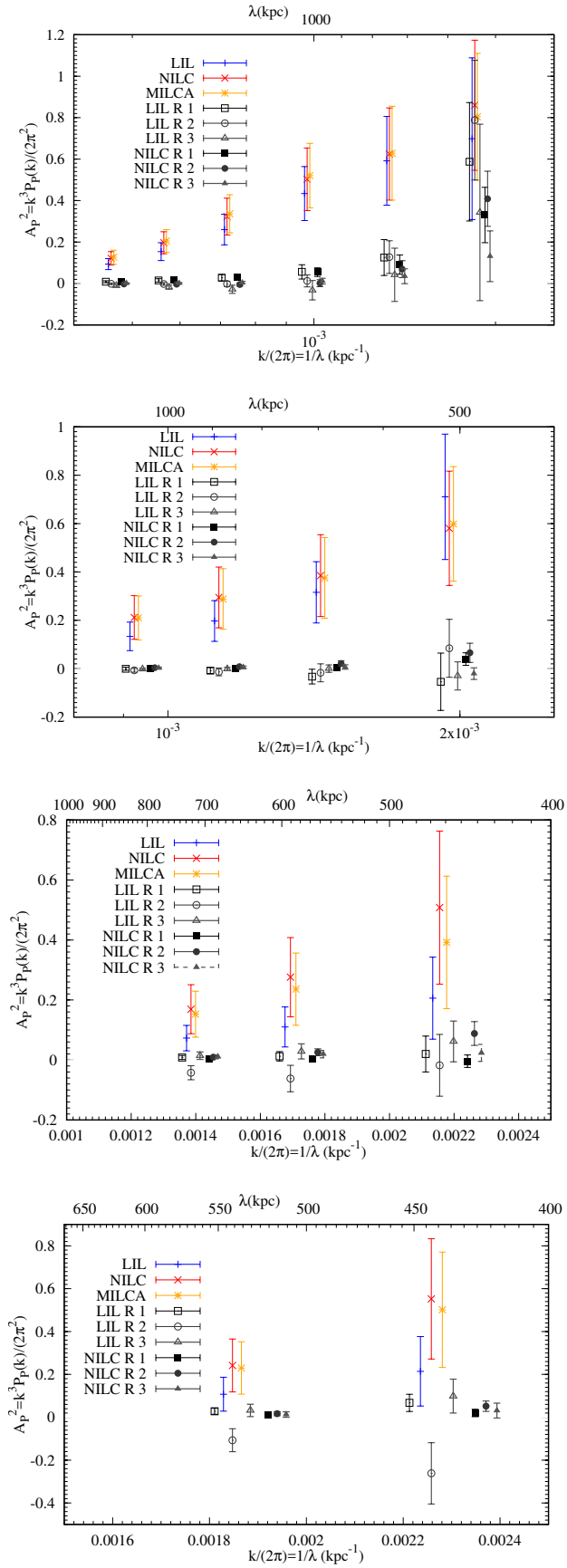


Figure 12. Squared amplitude spectrum of Coma pressure fluctuations for $\theta_{\rm max} = 60', 30', 20', 15'$ (top to bottom) in LIL, MILCA and NILC maps and in the test regions (LIL maps). For the test region we used our best fit Coma profile in the denominator to calculate $\delta y/\bar{y}$.

Table 1. Statistical properties of distribution of $\ln(1+\delta y/\bar{y})$ in the Coma cluster within radius of 60′ and 30′.

	Mean	Variance	Skewness	Kurtosis excess
LIL 60′	−0.054	0.26	−2.1	12.3
MILCA 60′	−0.1	0.24	−1.6	13.5
NILC 60′	−0.035	0.20	−1.1	11.3
LIL 30′	0.033	0.062	−0.73	3.23
MILCA 30′	−0.034	0.066	0.19	0.07
NILC 30′	0.035	0.060	0.54	−0.09

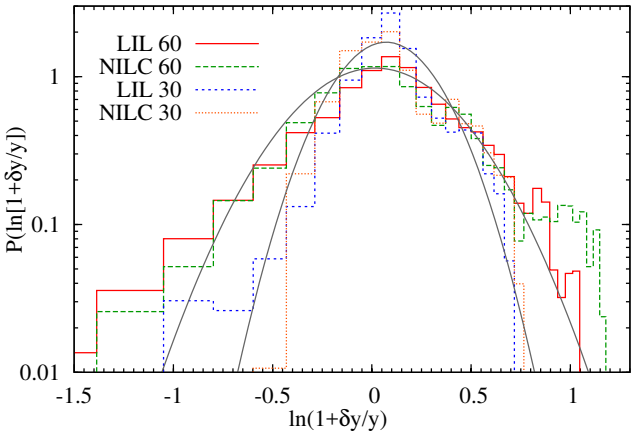


Figure 13. The PDF of SZ fluctuations in the Coma cluster within the 60′ and 30′ radius of the center in NILC and LIL maps. The distribution of $\ln(1+\delta y/\bar{y})$ is consistent with a Gaussian distribution (shown by solid gray lines) and therefore $\delta y/\bar{y}$ is consistent with having a log-normal distribution with mild non-Gaussianities (in $\ln(1+\delta y/\bar{y})$), which is also the statistics of thermodynamic perturbations driven by turbulence.

part of the Coma which cannot be fully explained by contribution due to contamination.

We plot the probability density function (PDF) of $\ln(1+\delta y/\bar{y})$ in Fig. 13 and the best fit normal distributions for 60′ and 30′ regions. The PDF of $\delta y/\bar{y}$ is approximately consistent with being a log-normal distribution. The properties of the distribution of $\ln(1+\delta y/\bar{y})$ (mean, variance, skewness, and kurtosis) are given in Table 1 for all three maps. The results from the three maps are again consistent with each other, especially for the mean and variance indicating that the contamination is sub-dominant. The spectra and related PDF have key implications for the ICM physics, which we discuss in depth in the next section.

3.1 Systematics due to ellipticity of the cluster

We have so far assumed spherical symmetry in our analysis. Clusters in the standard cosmological model are expected to be elliptical and this is indeed true for the Coma cluster (Schipper & King 1978; Neumann et al. 2003). If we try to fit a spherically or circularly symmetric profile to the ellipsoidal data, the residuals will look like anisotropies and may contribute to the fluctuation power spectrum. To study the amplitude of this effect we make an artificial elliptical cluster with similar β-profile as the Coma cluster and repeat all our steps on this simulated cluster. Neumann et al. (2003) have tried to fit an elliptical profile to the XMM-Newton observations getting eccentricities for the core of the cluster of $e = 0.4, 0.6$ for the pn and MOS data, respectively. We use the higher eccentricity as reference for our elliptical cluster model. We show the ellip-

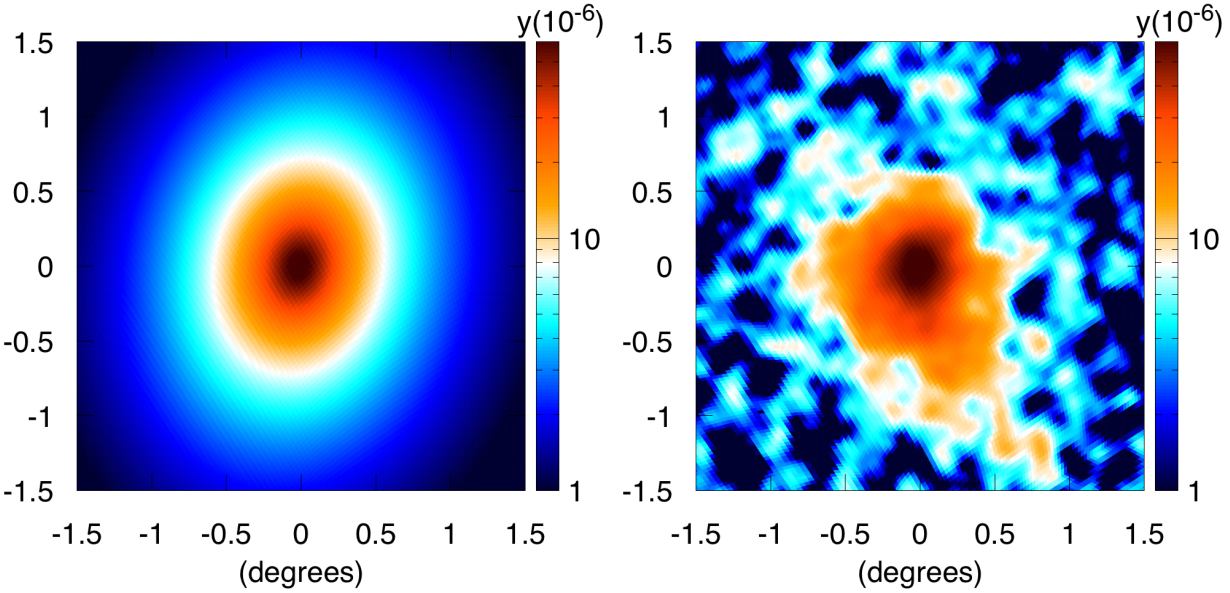


Figure 14. The elliptical cluster model (left) and Coma cluster in LIL map (right). We remark Coma cluster is less elliptical than our model with eccentricity $e = 0.6$. Therefore, the contribution to the power spectrum from ellipticity obtained from such model shall be seen as upper limits; in reality, we expect the ellipticity contributions to be much smaller.

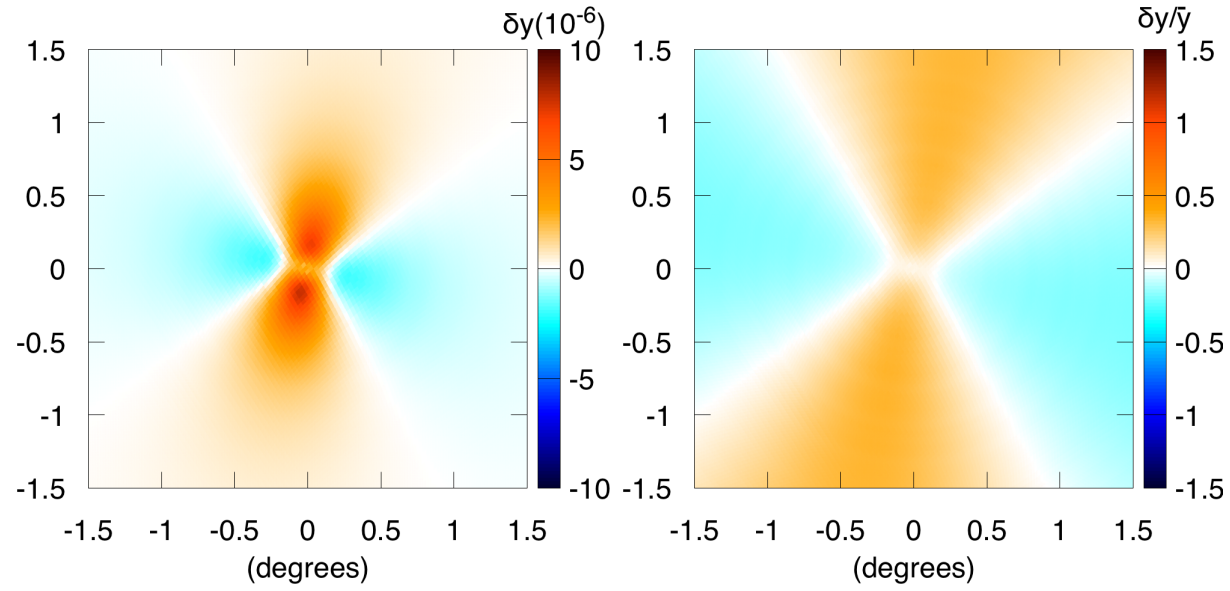


Figure 15. SZ fluctuations (left) and normalized fluctuations (right) for the elliptical cluster model. These maps should be compared with the corresponding Coma maps in Figs. 3 and 4.

tical model and Coma cluster in the LIL map in Fig. 14. We note Coma cluster gas distribution is much more complex than a simple elliptical profile and different radii have elongations along different directions. We then perform our previous analysis on such elliptical cluster model, subtracting the azimuthally averaged profile and retrieving δy and $\delta y/\bar{y}$ maps. These maps are shown in Fig. 15 and should be compared with the corresponding Coma maps in Figs. 3 and 4. The level of anisotropy introduced by ignoring the ellipticity is negligible compared with the actual fluctuations observed in the Coma cluster. In Fig. 16, we show the amplitude of the power spectrum of normalized fluctuations for the elliptical model cluster and compare it with the fluctuations in the Coma cluster in LIL map. Except for the innermost core, the contribution of ellipticity to the power spectrum is small (60' and 30' region) and can be ignored on small scales. For the core 15' region we are at the limit of resolution for the y map; there are indeed not enough pixels to make a definite statement about the ellipticity. In passing, we note that subtracting a spherical profile from an elliptical profile would result in a characteristic quadrupolar anisotropy which we do not see in the real Coma map. To summarize, the above results justify the

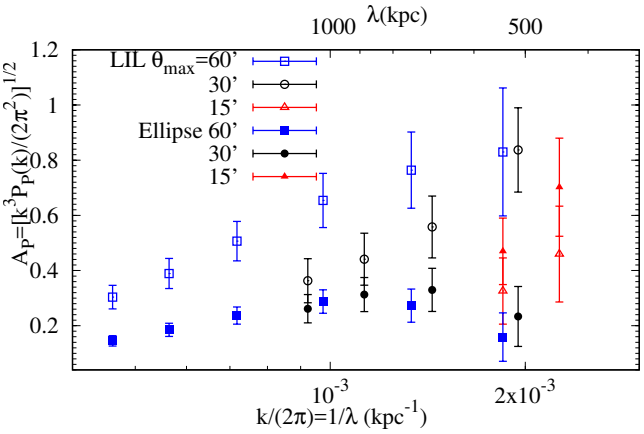


Figure 16. The amplitude of the power spectrum of the elliptical model compared with the measured fluctuations in Coma cluster.

usage of spherical symmetry and azimuthal averages in our fiducial analysis.

4 ICM PHYSICS: TURBULENCE, THERMODYNAMICS, HSE BIAS, AND COSMOLOGICAL IMPLICATIONS

As introduced in §1, the dominant scale and amplitude of the power spectrum allow us to probe the physics and (thermo)dynamics of the ICM plasma. The retrieved spectrum of pressure fluctuations at 500 kpc scale has an amplitude of 33 ± 12% in the inner 15′ extraction region of the cluster. The amplitude of pressure fluctuations at the same scale increases to 74 ± 19% if we use the 40′ radius region. Using previous Eq. 3 – which arises from the simulation modeling carried out in Gaspari & Churazov (2013) – and the adiabatic mode ($\delta P/P \simeq \gamma\,\delta\rho/\rho$; discussed below), we estimate that turbulence is characterized by 3-d Mach number $\mathrm{Ma}_{3\mathrm{d}} = 0.8 \pm 0.3$ (or $\mathrm{Ma}_{1\mathrm{d}} \approx 0.5 \pm 0.2$). This is larger value than the *Chandra* estimate since the new observational constraint on the amplitude peak has increased by 2×.[7] As the adiabatic sound speed is $c_s \simeq 1.5\times10^4\,T^{1/2} \simeq 1.5\times10^3\,\mathrm{km\,s^{-1}}$ ($T_0 = 8.5\,\mathrm{keV}$), the large-scale eddies have a characteristic velocity $\sigma_v \approx 1.2\times10^3\,\mathrm{km\,s^{-1}}$. For the 40′ region, we find $\mathrm{Ma}_{3\mathrm{d}} = 1.8 \pm 0.5$ if we extrapolate Eq. 3 to the supersonic regime, which is currently untested. We note that the temperature decreases down to 2 keV at 2 Mpc radius in Coma (Simionescu et al. 2013), therefore the physical velocities do not double as the Mach number does but increase by a much smaller amount, $\sigma_v \approx 1.8\times10^3$, while the compressibility of the medium progressively increases. The fact that at larger radial annuli the ICM reaches the transonic value is likely an indication that we are approaching the accretion shock region. Large-scale velocities up to a few $10^3\,\mathrm{km\,s^{-1}}$ are consistent with *Chandra* constraints derived from the redshift maps of 6 massive clusters undergoing significant merging activity (Liu et al. 2016), as well as large-scale cosmological simulations (e.g., Schmidt et al. 2016).

At scales larger than 500 kpc, the pressure fluctuations in all spectra (corresponding to different maximum extraction radii[8]) steadily decline, indicating a dominant turbulence injection scale at that location. The injection $L_{\mathrm{inj}} \simeq 500\,\mathrm{kpc}$ is consistent with gas motions driven by mergers and large-scale inflows, as indicated by cosmological simulations (e.g., Lau et al. 2009; Vazza et al. 2009, 2011; Miniati 2014)[9]. Even for the larger extraction region, the fluctuations power is mostly contained within $r < 1\,\mathrm{Mpc}$, i.e., well within the virial radius. Internal galaxy group merging and infall (e.g., Eckert et al. 2014; De Grandi et al. 2016) is thus the likely dominant driver compared to the large-scale cosmological filamentary accretion. Perturbations driven by the active galactic nucleus (AGN) feedback play a minor role, since the major AGN outflow outbursts can reach at best $0.1\,R_{500}$ (Gaspari et al. 2014b). The same can be said for perturbations linked to thermal instability (Gaspari 2015); besides Coma long cooling time, fluctuations related to thermal instability are typically contained within $r < 50\,\mathrm{kpc}$. External clumps accreted in the cluster outskirts may enhance density perturbations; however, recent cosmological simulations have shown that such 'clumpiness' is secondary compared with the perturbations imparted by non-thermal gas motions (Avestruz et al. 2016). For instance, the SW large-scale perturbation is cospatial with an infalling sub-structure (Neumann et al. 2001) which might in part increase the amplitude in the 60' spectrum; the 40' spectrum, on the other hand, excludes such region, showing a minor decrease in amplitude (< 20 percent; Sec. 3) and thus signaling that most of the power is contained in the chaotic motions.

Given the limited resolution of *Planck*, we are currently not able to constrain the small-scale ('inertial') slope of the power spectrum. The complementary X-ray data shows a quasi Kolmogorov power-law ($P_k \propto k^{-11/3}$, i.e., $A_k \propto k^{-1/3}$), classically related to turbulence with very low thermal conductivity. If we visually extrapolate the cascade beyond the *Chandra* peak (Fig. 11; cyan band), this joins within errorbars the *Planck* red/green data of the inner extraction regions (Fig. 11), in line with a self-similar cascade of turbulent eddies from L_{inj} to the dissipation scale (< 30 kpc). As warned in Gaspari & Churazov (2013), we remark the X-ray amplitude spectrum below $k < 5\times10^{-3}\,\mathrm{kpc^{-1}}$ is highly uncertain and can underestimate the perturbations, given the strong dependence of X-ray emissivity on radial distance ($\propto \rho^2$). A jump relative to SZ data is thus to be expected. Moreover, recall that *Planck* black/yellow/blue points cover much larger, more active extraction regions than that of *Chandra* (see Sec. 3). Higher resolution SZ observations are required to ensure tighter constraints on the full ICM power spectrum and to directly link the SZ observations to the X-ray data and related ICM microphysics. *Planck* data still add key value to our knowledge of the ICM physics, as it allows us to assess the global strength of internal motions and the ICM equation of state.

The distribution of SZ/pressure fluctuations follows a log-normal distribution with mild non-Gaussianities (fat tails and slight negative skewness; Fig. 13). Remarkably, turbulent motions drive thermodynamic perturbations (e.g., density, pressure) with similar log-normal statistics (Federrath et al. 2010; Gaspari et al. 2014a; Porter et al. 2015). Log-normal fluctuations in the ICM have been also found by X-ray studies on smaller scales (Kawahara et al. 2008). Regarding asymmetries, since the retrieved Coma Mach number is nearly transonic, a prediction from turbulence simulations (e.g., Kowal et al. 2007) is that stronger compressive motions

[7] We note that the injection scale can not be derived from the Gaspari & Churazov (2013) modeling, but must come from the observational data.

[8] Note that the scale λ (or Fourier mode k) is different from the radial distance r, the latter is the region used for calculating the power spectra while the former describes the wavelength of fluctuations.

[9] Nowadays it is still numerically unfeasible to resolve the long-term and 10s Mpc cosmological evolution, at the same time resolving turbulence and plasma physics down to the kpc scale over the whole cluster volume.

drive heavier tails, as found here. Overall, key signature of turbulence is to linearly drive the fluctuations rms $\sigma \propto \mathrm{Ma}_{3d}$ with log-normal and leptokurtic PDF, as we find in *Planck* data. This corroborates the importance of turbulence in shaping the dynamics of hot plasmas from the cosmological Mpc scale down to the kpc scales, and possibly further – below the Coulomb collisional scale – via kinetic plasma instabilities and Alfvén waves.

The *Planck* data helps us to constrain the dominant thermodynamic mode of the ICM. Since the retrieved gas motions are dynamically important ($\mathrm{Ma}_{3d} \gtrsim 0.8$), perturbations are expected to drift toward the adiabatic regime (Gaspari et al. 2014a), i.e., $\delta P/P = \gamma\,\delta\rho/\rho$, the regime adopted in Fig. 11. This is valid for $\mathrm{Ma}_{3d} > 0.5$. The fact that we see substantial pressure fluctuations indicates by itself that Coma cluster is globally not in isobaric mode, at least at intermediate and large scales. In such regime, sound waves (linked to pressure fluctuations) start to overcome pure entropy perturbations (mediated by buoyancy/gravity waves). The latter regime would dominate if $\mathrm{Ma}_{3d} \ll 0.5$ with $\delta K/K \gg \delta P/P$, where $\delta K/K$ are the entropy perturbations (see Gaspari et al. 2014a for an in-depth theoretical derivation). This is corroborated by the aforementioned cosmological simulations, showing that the cosmological accretion inflow and mergers drive turbulence with average kinetic energy 5 - 35% of the thermal energy, from relaxed to unrelaxed clusters (e.g., Vazza et al. 2011). Using our turbulence constraint, Coma has turbulent energy density in the inner region

$$E_{\rm turb} \equiv \frac{1}{2}\rho\sigma_v^2 = \frac{1}{2}\gamma(\gamma-1)\,\mathrm{Ma}_{3d}^2\,E_{\rm th} \simeq 0.34 \pm 0.25\,E_{\rm th}. \quad (10)$$

If we consider the 1 Mpc radius region, the turbulent energy becomes comparable to the thermal energy, although it should be kept in mind the large error bars. As expected, Coma belongs to the class of unrelaxed clusters with a major dynamic component.

Besides difficult lensing estimates, cluster masses are typically retrieved via the X-ray density and temperature radial profile assuming hydrostatic equilibrium (HSE), $\mathrm{d}P_{\rm tot}/\mathrm{d}r = -\rho\,GM(<r)/r^2$, where G is the gravitational constant, $P_{\rm tot}$ is the total pressure – thermal and non-thermal – and $M(<r)$ is the mass enclosed within radius r. Expanding the previous equation, the total mass can be retrieved as

$$M_{\rm tot}(<r) = -\frac{k_{\rm B}T(r)\,r}{\mu m_{\rm p}\,G}\left[\frac{\mathrm{d}\ln\rho(r)}{\mathrm{d}\ln r} + \frac{\mathrm{d}\ln T(r)}{\mathrm{d}\ln r} + \frac{P_{\rm nt}}{P}\frac{\mathrm{d}\ln P_{\rm nt}}{\mathrm{d}\ln r}\right], \quad (11)$$

where the last term is the non-thermal pressure support which is not included in observed X-ray masses $M_{\rm x}$, μ is the mean atomic weight and m_p is the proton mass. The mass bias is thus

$$b_{\rm M} \equiv \frac{M_{\rm x}}{M_{\rm tot}} - 1 = -\frac{P_{\rm nt}}{P}\frac{\mathrm{d}\ln P_{\rm nt}}{\mathrm{d}\ln P}\left(1 + \frac{P_{\rm nt}}{P}\frac{\mathrm{d}\ln P_{\rm nt}}{\mathrm{d}\ln P}\right)^{-1}, \quad (12)$$

Since $P = (\gamma-1)\,E_{\rm th} = (2/3)\,E_{\rm th}$ and $P_{\rm nt} = (1/3)\rho\sigma_v^2 = (2/3)E_{\rm nt}$ (e.g., Lau et al. 2009; Schmidt et al. 2016), thus $P_{\rm nt}/P = (\gamma/3)\,\mathrm{Ma}_{3d}^2$ and

$$\frac{\mathrm{d}\ln P_{\rm nt}/\mathrm{d}\ln r}{\mathrm{d}\ln P/\mathrm{d}\ln r} = 1 + 2\,\frac{\mathrm{d}\ln \mathrm{Ma}_{3d}/\mathrm{d}\ln \mathrm{r}}{\mathrm{d}\ln P/\mathrm{d}\ln r}. \quad (13)$$

Beyond the core radius, the pressure gradient slope is $-2\,(\beta+1/2) \simeq -3.14$ (Eq. 5) and our retrieved Mach between the 40' and 15' radius implies $\mathrm{d}\ln \mathrm{Ma}_{3d}/\mathrm{d}\ln r \simeq 0.8$, yielding a mass bias

$$b_{\rm M} \simeq -0.27\,\mathrm{Ma}_{3d}{}^2\left(1 + 0.27\,\mathrm{Ma}_{3d}^2\right)^{-1} \simeq -15\% \div -45\%, \quad (14)$$

for the inner (15') and outskirt (40') region, respectively. The substantial increase in non-equilibrium measures at larger radii is consistent with large-scale cosmological simulations (e.g., Battaglia et al. 2015). The above analysis accounts only for turbulence as the dominant source of non-thermal pressure; magnetic fields and cosmic rays may further increase the bias. Bonafede et al. (2010) find a weak 1 - 5 μG magnetic field in Coma cluster (from the outskirts to the core, respectively) by using Faraday rotation measure in radio data. The magnetic pressure, $B^2/(8\pi)$, is thus < 10 percent of our retrieved turbulent pressure.

Although we analyzed only one cluster, the HSE bias is expected to play a crucial role in the mass estimates of all cosmological systems, from massive clusters to galaxy groups (e.g., Rasia et al. 2004; Lau et al. 2009; Sun et al. 2009). Moreover, it is well known that cosmological parameter constraints (such as σ_8) derived from SZ clusters and CMB are in tension (Planck Collaboration et al. 2015c). For instance, Shaw et al. (2010) show that increasing the fraction of $P_{\rm nt}$ support in the ICM reduces the total SZ power and can thus alleviate such tension (see also de Haan et al. 2016). Furthermore, retrieving true masses allows us to accurately assess the main scaling relations of virialized structures (in terms of both slope and intrinsic scatter), such as $L_{\rm x} - M_{\rm tot}$ and $M_{\rm tot} - T_{\rm x}$, where $L_{\rm x}$ is the X-ray luminosity and $T_{\rm x}$ is the X-ray temperature, typically within R_{500} (Giodini et al. 2013 for a review). In conclusion, while total SZ power probes the thermal energy content, the related SZ fluctuations tell us the strength of the non-thermal deviations, thus providing a global, self-consistent view of the cluster (thermo)dynamics.

5 CONCLUSIONS

We have for the first time used the thermal Sunyaev-Zeldovich effect to constrain the absolute and relative y fluctuations. Such fluctuations put key constraints on the physics of the intracluster medium, such as turbulence and the dominant thermodynamics, with major implications for cosmological studies. We applied our methodology to the archetypal massive galaxy cluster Coma (Abell 1656), which can be replicated for any other system hosting a hot gaseous halo. Our major conclusions are summarized as follows.

- Relative 3-d pressure perturbations $\delta P/P$ can be retrieved via the 2-d SZ perturbations $\delta y/y$, after removal of the average background profile and spherical deprojection. The retrieved pressure fluctuations peak at 500 kpc, which is at the limit of Planck resolution, and steadily decline beyond 1 Mpc. When combined with the decline in X-ray derived power spectrum on smaller scales, we can take it as an evidence for a peak in the turbulence power spectrum at $\approx$500 kpc scales. The fluctuations at such dominant scale are $\delta P/P = 33 \pm 12\%$ and $74 \pm 19\%$ for the 15′ and 40′ radius region, respectively. Because of the limited angular resolution, *Planck* can not resolve the power-law cascade in the spectrum, which is instead constrained by X-ray *Chandra* data ($A_k \propto k^{-1/3}$; Kolmogorov slope).

- We carefully tested the impact of foreground/background contamination, selecting external regions without evident structures, and we provided evidence that intrinsic SZ perturbations, and not contamination, dominate our signal within Coma cluster, in particular within $r < 1$ Mpc.

- We show how to deproject the SZ fluctuations in Fourier space. The impact of projection effects is to suppress the small scale power as a function of the SZ window function $W(\theta, z)$, which is broader than that of X-ray emissivity ($\propto n^2$). The 3-d to 2-d amplitude ratio however does not vary drastically: it is of order

unity at Mpc scale, increasing by a factor of a few at smaller scales.

- SZ fluctuations are a novel important tool to probe the ICM physics, which optimally complements the X-ray data tied to smaller tens of kpc scales. By using the modeling and 3-d high-resolution simulations presented in Gaspari et al. (2013; 2014a), which relate turbulence to thermodynamic perturbations, we improve the turbulence constraints in Coma. The turbulence Mach number is $\mathrm{Ma}_{3d} = 0.8 \pm 0.3$ (15' region) with injection scale $L_{\rm inj} \approx 500$ kpc. For the 40' region, the Mach number doubles, albeit velocities remain similar due to the declining plasma temperature. The transonic value at larger radii suggests that we are approaching the accretion shock region.

- The large SZ fluctuations imply that the hot halo is in adiabatic mode (mediated by sound waves), rather than in isobaric mode (mediated by buoyancy waves). The large injection scale and velocities ≈ 1.2 - 1.8×10^3 km s^{-1} are consistent with driving due to mergers, in particular tied to internal galaxy groups – in agreement with cosmological simulations and complementary X-ray data.

- The PDF of SZ fluctuations is log-normal with mild non-Gaussianities (heavier tails). This is the same statistics of perturbations predicted by high-resolution simulations of turbulence, with heavier tails induced by the increasingly compressive motions (since approaching the transonic regime).

- The non-thermal pressure support is $E_{\rm turb}/E_{\rm th} \simeq 0.34$ (for 15' radius), corroborating Coma belongs to the class of unrelaxed clusters. We propose a simple methodology (Eq. 12-14) to study the mass bias $b_M = M_{\rm x}/M - 1$ as a function of Mach number. The retrieved turbulent pressure can induce significant HSE mass bias $b_M \approx -15\%$ to -45% in the core and cluster outskirts, respectively. The SZ fluctuations spectrum thus allows to better retrieve the true masses, improving our ability to carry out precision cosmology, in terms of measuring the cosmological parameters (e.g., σ_8) and the main scaling relations (e.g., $L_{\rm x} - M_{\rm tot}$, $M_{\rm tot} - T_{\rm x}$).

This study opens up a new window into the diffuse gas/plasma physics. While total SZ power conveys the total energy content, the SZ fluctuations unveil the non-thermal deviations, thus providing a self-consistent way to assess the global cluster thermodynamics. The ground based high-resolution SZ missions – SPT (J. J. McMahon et al. 2009), ALMA (Yamada et al. 2012), ACT (Niemack et al. 2010), CARMA (Rodríguez-Gonzálvez et al. 2015), Mustang (Dicker et al. 2014) – will be able to extend our work based on *Planck* maps and assess the full cascade of perturbations. Future CMB space experiments as COrE (The COrE Collaboration 2011; Cosmic Origins Explorer) and PRISM (Polarized Radiation Imaging and Spectroscopy Mission; P. Andre et al. 2014) may even probe the small scales accessible to X-ray, due to the better S/N and foreground cleaning. Considering that, at the present time, the next large X-ray mission *Athena* has foreseen launch in 2028, the aforementioned SZ missions are vital to advance cluster astrophysics. In closing, we remark the importance of combining multi-wavelength observations and multi-scale simulations, as probing the astrophysics of the diffuse gas and hot plasmas is inevitably tied to cosmological studies, and vice versa.

ACKNOWLEDGEMENTS

This paper used observations obtained with *Planck* (http://www.esa.int/Planck), an ESA science mission with instruments and contributions directly funded by ESA Member States, NASA, and Canada. This research also made use of the HEALPix software (Górski et al. 2005) (http://healpix.sourceforge.net) and *Aladin sky atlas* developed at CDS, Strasbourg Observatory, France (Bonnarel et al. 2000). M.G. is supported by NASA through Einstein Postdoctoral Fellowship Award Number PF-160137 issued by the Chandra X-ray Observatory Center, which is operated by the Smithsonian Astrophysical Observatory for and on behalf of NASA under contract NAS8-03060. This work made use of the computational resources of Department of Theoretical Physics, TIFR. We thank D. Eckert, N. Battaglia, D. Spergel, J. Stone, S. Molendi, F. Gastaldello, E. Pointecouteau, E. Churazov for helpful comments. We are grateful to the referee for the detailed insights which helped to improve the manuscript.

REFERENCES

Abell G. O., Corwin Jr. H. G., Olowin R. P., 1989, ApJS, 70, 1
Anderson M. E., Gaspari M., White S. D. M., Wang W., Dai X., 2015, MNRAS, 449, 3806
Avestruz C., Nagai D., Lau E. T., 2016, preprint, (arXiv:1605.01723)
Battaglia N., Bond J. R., Pfrommer C., Sievers J. L., 2012, ApJ, 758, 75
Battaglia N., Bond J. R., Pfrommer C., Sievers J. L., 2015, ApJ, 806, 43
Biffi V., et al., 2016, ApJ, 827, 112
Bonafede A., Feretti L., Murgia M., Govoni F., Giovannini G., Dallacasa D., Dolag K., Taylor G. B., 2010, A&A, 513, A30
Bonnarel F., et al., 2000, A&A Supp., 143, 33
Briel U. G., Henry J. P., Boehringer H., 1992, A&A, 259, L31
Chaudhuri A., Nath B. B., Majumdar S., 2012, ApJ, 759, 87
Chaudhuri A., Majumdar S., Nath B. B., 2013, ApJ, 776, 84
Chon G., Challinor A., Prunet S., Hivon E., Szapudi I., 2004, MNRAS, 350, 914
Churazov E., et al., 2012, MNRAS, 421, 1123
De Grandi S., et al., 2016, preprint, (arXiv:1602.07148)
Delabrouille J., Cardoso J.-F., Le Jeune M., Betoule M., Fay G., Guilloux F., 2009, A&A, 493, 835
Dicker S. R., et al., 2014, Journal of Low Temperature Physics, 176, 808
Dolag K., Vazza F., Brunetti G., Tormen G., 2005, MNRAS, 364, 753
Eckert D., et al., 2014, A&A, 570, A119
Erler J., Basu K., Trasatti M., Klein U., Bertoldi F., 2015, MNRAS, 447, 2497
Federrath C., Banerjee R., Clark P. C., Klessen R. S., 2010, ApJ, 713, 269
Ferrari C., Govoni F., Schindler S., Bykov A. M., Rephaeli Y., 2008, Space Sci. Rev., 134, 93
Fox D. C., Pen U.-L., 2002, ApJ, 574, 38
Gaspari M., 2015, MNRAS, 451, L60
Gaspari M., Churazov E., 2013, A&A, 559, A78
Gaspari M., Churazov E., Nagai D., Lau E. T., Zhuravleva I., 2014a, A&A, 569, A67
Gaspari M., Brighenti F., Temi P., Ettori S., 2014b, ApJL, 783, L10
Gaspari M., Brighenti F., Temi P., 2015, A&A, 579, A62
Giodini S., Lovisari L., Pointecouteau E., Ettori S., Reiprich T. H., Hoekstra H., 2013, SSRv, 177, 247
Górski K. M., Hivon E., Banday A. J., Wandelt B. D., Hansen F. K., Reinecke M., Bartelmann M., 2005, ApJ, 622, 759
Hallman E. J., Burns J. O., Motl P. M., Norman M. L., 2007, ApJ, 665, 911
Hill J. C., Spergel D. N., 2014, JCAP, 2, 30
Hivon E., Górski K. M., Netterfield C. B., Crill B. P., Prunet S., Hansen F., 2002, ApJ, 567, 2
Hofmann F., Sanders J. S., Nandra K., Clerc N., Gaspari M., 2016, A&A, 585, A130
Hurier G., Macías-Pérez J. F., Hildebrandt S., 2013, A&A, 558, A118

Iapichino L., Schmidt W., Niemeyer J. C., Merklein J., 2011, MNRAS, 414, 2297
J. J. McMahon et al. 2009, in Young B., Cabrera B., Miller A., eds, American Institute of Physics Conference Series Vol. 1185, American Institute of Physics Conference Series. pp 511–514, doi:10.1063/1.3292391
Jaffe A. H., Kamionkowski M., 1998, Phys.Rev.D, 58, 043001
Kawahara H., Reese E. D., Kitayama T., Sasaki S., Suto Y., 2008, ApJ, 687, 936
Khatri R., 2015, MNRAS, 451, 3321
Khatri R., 2016, A&A, 592, A48
Khatri R., Sunyaev R., 2015, JCAP, 8, 013
Kowal G., Lazarian A., Beresnyak A., 2007, ApJ, 658, 423
Lau E. T., Kravtsov A. V., Nagai D., 2009, ApJ, 705, 1129
Liu A., Yu H., Tozzi P., Zhu Z.-H., 2016, preprint, (arXiv:1602.07704)
Mahdavi A., Hoekstra H., Babul A., Henry J. P., 2008, MNRAS, 384, 1567
Miniati F., 2014, ApJ, 782, 21
Nelson K., Lau E. T., Nagai D., Rudd D. H., Yu L., 2014, ApJ, 782, 107
Neumann D. M., et al., 2001, A&A, 365, L74
Neumann D. M., Lumb D. H., Pratt G. W., Briel U. G., 2003, A&A, 400, 811
Niemack M. D., et al., 2010, in Millimeter, Submillimeter, and Far-Infrared Detectors and Instrumentation for Astronomy V. p. 77411S (arXiv:1006.5049), doi:10.1117/12.857464
P. Andre et al. 2014, JCAP, 2, 6
Peacock J. A., 1999, Cosmological Physics. Cambridge University Press
Peebles P. J. E., Yu J. T., 1970, ApJ, 162, 815
Plagge T., et al., 2010, ApJ, 716, 1118
Planck Collaboration et al., 2011, A&A, 536, A1
Planck Collaboration et al., 2013, A&A, 554, A140
Planck Collaboration et al., 2015a, preprint, (arXiv:1502.01596)
Planck Collaboration et al., 2015c, preprint, (arXiv:1502.01597)
Planck Collaboration et al., 2015e, preprint, (arXiv:1507.02058)
Planck Collaboration et al., 2015b, preprint, (arXiv:1502.01598)
Planck Collaboration et al., 2015d, preprint, (arXiv:1511.05156)
Porter D. H., Jones T. W., Ryu D., 2015, ApJ, 810, 93
Rasia E., Tormen G., Moscardini L., 2004, MNRAS, 351, 237
Rodríguez-Gonzálvez C., Muchovej S., Chary R. R., 2015, MNRAS, 447, 902
Ruan J. J., McQuinn M., Anderson S. F., 2015, ApJ, 802, 135
Sanders J. S., Fabian A. C., 2012, MNRAS, 421, 726
Schellenberger G., Reiprich T. H., Lovisari L., Nevalainen J., David L., 2015, A&A, 575, A30
Schipper L., King I. R., 1978, ApJ, 220, 798
Schmidt W., Engels J. F., Niemeyer J. C., Almgren A. S., 2016, MNRAS,
Schuecker P., Finoguenov A., Miniati F., Böhringer H., Briel U. G., 2004, A&A, 426, 387
Shaw L. D., Nagai D., Bhattacharya S., Lau E. T., 2010, ApJ, 725, 1452
Shi X., Komatsu E., Nelson K., Nagai D., 2015, MNRAS, 448, 1020
Simionescu A., et al., 2013, ApJ, 775, 4
Smith G. P., et al., 2016, MNRAS, 456, L74
Sun M., Voit G. M., Donahue M., Jones C., Forman W., Vikhlinin A., 2009, ApJ, 693, 1142
Sunyaev R. A., Zeldovich Y. B., 1970, ApSS, 7, 3
Sunyaev R. A., Zeldovich Y. B., 1972, Comments on Astrophysics and Space Physics, 4, 173
Szapudi I., Prunet S., Colombi S., 2001, ApJL, 561, L11
The COrE Collaboration 2011, preprint, (arXiv:1102.2181)
Tristram M., Macías-Pérez J. F., Renault C., Santos D., 2005, MNRAS, 358, 833
Vazza F., Brunetti G., Kritsuk A., Wagner R., Gheller C., Norman M., 2009, A&A, 504, 33
Vazza F., Brunetti G., Gheller C., Brunino R., Brüggen M., 2011, A&A, 529, A17
Yamada K., et al., 2012, PASJ, 64
Zeldovich Y. B., Sunyaev R. A., 1969, ApSS, 4, 301
Zhang Y.-Y., et al., 2010, ApJ, 711, 1033
Zhuravleva I., Churazov E., Kravtsov A., Sunyaev R., 2012, MNRAS, 422, 2712
de Haan T., et al., 2016, preprint, (arXiv:1603.06522)
von der Linden A., et al., 2014, MNRAS, 443, 1973

APPENDIX A: FLAT SKY APPROXIMATION

We review the flat sky approximation following Jaffe & Kamionkowski (1998). Let us consider the correlation function written in terms of Fourier space as well as in spherical harmonic space. Equating the two ways of calculating the same correlation function gives us the flat sky relation between the two power spectra.

We will use angular brackets to denote ensemble average. In flat space two dimensional Cartesian position vector is $\mathbf{x} = (x\cos\phi, x\sin\phi)$, where the bold font denotes a vector and normal font its scalar amplitude. The correlation function for a field $f(\mathbf{x})$ for two points separated by displacement vector $\mathbf{r}$ is, assuming statistical homogeneity,

$$\begin{aligned} C(r) &\equiv \langle f(\mathbf{x}+\mathbf{r})f(\mathbf{x})\rangle \\ &= \int \frac{\mathrm{d}^2k}{(2\pi)^2} \mathrm{e}^{i\mathbf{k}.\mathbf{x}} \frac{\mathrm{d}^2k'}{(2\pi)^2} \mathrm{e}^{i\mathbf{k}'.(\mathbf{x}+\mathbf{r})} \langle f(\mathbf{k})f(\mathbf{k}')\rangle \\ &= \int \frac{\mathrm{d}^2k}{(2\pi)^2} \mathrm{e}^{-i\mathbf{k}.\mathbf{r}} P_f(k) \\ &= \int \frac{k\mathrm{d}k\mathrm{d}\phi_k}{(2\pi)^2} \mathrm{e}^{-ikr(\cos\phi_k\cos\phi+\sin\phi_k\sin\phi)} P_f(k) \\ &= \int \frac{k\mathrm{d}k}{2\pi} J_0(kr) P_f(k), \end{aligned} \tag{A1}$$

where we have used $\mathbf{k} = (k\cos\phi_k, k\sin\phi_k)$, $\langle f(\mathbf{k})f(\mathbf{k}')\rangle = (2\pi)^2\delta_D(\mathbf{k}_{\mathbf{k}'})P_f(k)$, δ_D is the Dirac delta distribution, and $P_f(k)$ is the Fourier space power spectrum. In the last line we integrated over the Fourier angle ϕ_k and J_0 is the Bessel function of first kind.

Doing the same exercise on a sphere of radius R so that $r = R\theta$, and θ is the angular distance between the two points on the sphere, we get

$$C(r) = C(R\theta) = \sum_\ell \frac{2\ell+1}{4\pi} \mathcal{P}_\ell(\cos(\theta)) C_\ell \tag{A2}$$

Using the fact that for $\ell \gg 1$ we have $\mathcal{P}_\ell(\cos(\theta)) \approx J_0(\ell\theta)$ and approximating the sum by an integral we get

$$C(r) \approx \int \frac{\ell\mathrm{d}\ell}{2\pi} J_0\left(\frac{\ell r}{R}\right) C_\ell \tag{A3}$$

From Eqs. A1 and A3 we get $k^2P_f(k) \approx \ell^2 C_\ell|_{\ell=kR}$. Note that k in our convention is the angular frequency with $k = 2\pi/\lambda$, where λ is the physical wavelength of the Fourier mode. We use PolSpice software package (Szapudi et al. 2001; Chon et al. 2004) software package which calculates the power spectra in the spherical harmonic domain and use the flat sky approximation to present the results in the Fourier domain. Note that since we have data on a sphere, spherical harmonics are the natural basis for analyzing the data.

APPENDIX B: RELATION BETWEEN PRESSURE AND SZ POWER SPECTRUM ASSUMING SPHERICAL SYMMETRY

We can get the relationship between the pressure and SZ power spectrum under the assumption of spherical symmetry by calculating the correlation function in two different ways. For the SZ

correlation between two points at $\boldsymbol{\theta}$ and $\boldsymbol{\theta}+\mathbf{r}$ we have

$$C(r) \equiv \langle \frac{\delta y}{y}(\boldsymbol{\theta}) \frac{\delta y}{y}(\boldsymbol{\theta}+\mathbf{r}) \rangle = \int \frac{\mathrm{d}^2 k_\theta}{(2\pi)^2} \mathrm{e}^{i\mathbf{k}_\theta.\boldsymbol{\theta}} \frac{\mathrm{d}^2 k'_\theta}{(2\pi)^2} \mathrm{e}^{i\mathbf{k}'_\theta.(\boldsymbol{\theta}+\mathbf{r})} \langle \tilde{y}(\mathbf{k}_\theta) \tilde{y}(\mathbf{k}'_\theta) \rangle$$
$$= \int \frac{\mathrm{d}^2 k_\theta}{(2\pi)^2} \mathrm{e}^{-i\mathbf{k}_\theta.\mathbf{r}} P_y(k_\theta), \tag{B1}$$

where $\tilde{y}$ is the Fourier transform of $\frac{\delta y}{y}$ and we have used

$$\langle \tilde{y}(\mathbf{k}_\theta) \tilde{y}(\mathbf{k}'_\theta) \rangle = (2\pi)^2 P_y(k_\theta) \delta_D^2(\mathbf{k}_\theta + \mathbf{k}'_\theta), \tag{B2}$$

and δ_D is the Dirac delta distribution. Alternatively we can write y as integral over pressure along the line of sight direction which we take along the z direction,

$$C(r) \equiv \langle \frac{\delta y}{\bar{y}}(\boldsymbol{\theta}) \frac{\delta y}{\bar{y}}(\boldsymbol{\theta}+\mathbf{r}) \rangle = \langle \frac{\int \bar{P}(\delta P/\bar{P}) \mathrm{d}z}{\int \bar{P} \mathrm{d}z}(\boldsymbol{\theta}) \frac{\int \bar{P}(\delta P/\bar{P}) \mathrm{d}z}{\int \bar{P} \mathrm{d}z}(\boldsymbol{\theta}+\mathbf{r}) \rangle \tag{B3}$$

Defining the window function

$$W(z) \equiv \frac{\bar{P}}{\int \bar{P} \mathrm{d}z} = \frac{m_\mathrm{e} c^2}{\sigma_\mathrm{T}} \frac{\bar{P}}{\bar{y}} \tag{B4}$$

and assuming that it is independent of $\boldsymbol{\theta}$, we get

$$C(r) = \langle \int \mathrm{d}z\, W \frac{\delta P}{\bar{P}}(\boldsymbol{\theta}) \int \mathrm{d}z' W \frac{\delta P}{\bar{P}}(\boldsymbol{\theta}+\mathbf{r}) \rangle$$
$$= \int \mathrm{d}z \mathrm{d}z' \frac{\mathrm{d}^3 k}{(2\pi)^3} \frac{\mathrm{d}^3 k'}{(2\pi)^3} \frac{\mathrm{d}k'_{z_1}}{2\pi} \frac{\mathrm{d}k'_{z_2}}{2\pi} \tilde{W}\left(k_z - k'_{z_1}\right) \tilde{W}\left(k'_z - k'_{z_2}\right)$$
$$\mathrm{e}^{i\left(\mathbf{k}_\theta.\boldsymbol{\theta} + k_z.z + \mathbf{k}'_\theta.(\boldsymbol{\theta}+\mathbf{r}) + k'_z.z'\right)} \langle \tilde{P}\left(\mathbf{k}_\theta, k'_{z_1}\right) \tilde{P}\left(\mathbf{k}'_\theta, k'_{z_2}\right) \rangle, \tag{B5}$$

where we have defined $\tilde{P}$ as the Fourier transform of $\delta P/\bar{P}$ and $\tilde{W}$ as the Fourier transform of W. Using

$$\langle \tilde{P}\left(\mathbf{k}_\theta, k'_{z_1}\right) \tilde{P}\left(\mathbf{k}'_\theta, k'_{z_2}\right) \rangle = (2\pi)^3 \delta_D^2\left(\mathbf{k}_\theta + \mathbf{k}'_\theta\right) \delta_D\left(k'_{z_1} + k'_{z_2}\right) P_p\left(\left|\mathbf{k}_\theta + \mathbf{k}'_{\mathbf{z}_1}\right|\right) \tag{B6}$$

and integrating using the Dirac delta distributions we get

$$C(r) = \int \frac{\mathrm{d}^2 k_\theta}{(2\pi)^2} \frac{\mathrm{d}k_z}{2\pi} \left|\tilde{W}(k_z)\right|^2 \mathrm{e}^{i\mathbf{k}_\theta.\mathbf{r}} P_p\left(|\mathbf{k}_\theta + \mathbf{k}_\mathbf{z}|\right) \tag{B7}$$

Comparing with Eq. B1 we get the relation between the 2-d and 3-d power spectrum

$$P_y(k_\theta) = \int \frac{\mathrm{d}k_z}{2\pi} \left|\tilde{W}(k_z)\right|^2 P_p\left(|\mathbf{k}_\theta + \mathbf{k}_\mathbf{z}|\right) \tag{B8}$$

APPENDIX C: FOURIER CONVENTION

We have used the Fourier convention where the reverse transform is given by (in n dimensions)

$$f(\mathbf{x}) = \int \frac{\mathrm{d}^n k}{(2\pi)^n} \tilde{f}(\mathbf{k}) \mathrm{e}^{i\mathbf{k}.\mathbf{x}} \tag{C1}$$

X-ray studies typically use the Fourier convention (e.g., Churazov et al. 2012; Zhuravleva et al. 2012; Gaspari & Churazov 2013)

$$f(\mathbf{x}) = \int \mathrm{d}^n q\, \tilde{f}(\mathbf{q}) \mathrm{e}^{i2\pi\mathbf{q}.\mathbf{x}}, \tag{C2}$$

where $q = k/(2\pi)$. The power per unit logarithmic frequency interval, A, is dimensionless and independent of the Fourier convention used. By equating the real space variance, $C(0) \equiv \langle f(\mathbf{x}) f(\mathbf{x}) \rangle$, as in the previous section, we get the relation between the power spectrum in the two conventions as (with the subscript k or q specifying the Fourier convention)

$$A_q = \sqrt{4\pi q^3 P_q(q)} = A_k = \sqrt{\frac{k^3}{2\pi^2} P_k(k)} \tag{C3}$$

in 3-d and

$$A_q = \sqrt{2\pi q^2 P_q(q)} = A_k = \sqrt{\frac{k^2}{2\pi} P_k(k)} \tag{C4}$$

in 2-d. The Fourier conventions for the power spectrum in n dimensions are

$$\langle \tilde{f}(\mathbf{q}) \tilde{f}(\mathbf{q}') \rangle = \delta_D^n(\mathbf{q} - \mathbf{q}') P_q(q)$$
$$\langle \tilde{f}(\mathbf{k}) \tilde{f}(\mathbf{k}') \rangle = (2\pi)^n \delta_D^n(\mathbf{k} - \mathbf{k}') P_k(k), \tag{C5}$$

where δ_D^n is the n-dimensional Dirac delta distribution.